From plasmodesma geometry to effective symplastic permeability through biophysical modelling

Eva E. Deinum[1*], **Yoselin Benitez-Alfonso**[2†], **Bela M. Mulder**[3,4†]

***For correspondence:**
eva.deinum@wur.nl (EED)

[†]These authors contributed equally to this work

[1]Mathematical and statistical methods (Biometris), Wageningen University, Wageningen, 6708 PB, the Netherlands; [2]Centre for Plant Science, School of Biology, University of Leeds, Leeds LS2 9JT, UK; [3]Living Matter Department, Institute AMOLF, Amsterdam, 1098 XG, the Netherlands; [4]Laboratory of Cell Biology, Wageningen University, Wageningen, 6708 PB, the Netherlands

Abstract Regulation of molecular transport via intercellular channels called plasmodesmata (PDs) is important for both, the coordination of developmental and environmental responses among neighbouring cells and the isolation of cell domains to execute specific developmental or stress-induced programs. PD transport capacity (i.e. effective symplastic permeability) has been determined experimentally, at a tissue level, by assessing the mobility of different fluorescent molecules, or predicted from PD ultrastructural features using electron-microscopy. Values obtained from these approaches are often very different. Here, we build a theoretical bridge between the two experimental approaches by calculating the effective symplastic permeability from a geometrical description of individual PDs, considering the flow towards them and including the impact of PD clustering into pit fields. Our open source multi-level model allows us to link measured permeabilities with realistic PD dimensions, predict how typical PD features affect transport properties and add a functional interpretation to recent experimental observations.

Introduction

The formation of spatial patterns in plants requires the transport and interaction of molecular signals. This sharing of information coordinates cell fate decisions over multiple cells and the isolation of cell fate determinants within a cell or group of cells on the same developmental path. Small molecules such as sugars, peptides, hormones and RNAs move long and short distances to coordinate cell/organ development (***Otero et al., 2016***). Cell-to-cell transport of proteins, such as transcription factors, is also important in the regulation and/or developmental reprogramming of local cellular domains (***Gallagher et al., 2014***). A well studied example is SHORT-ROOT (SHR), an *Arabidopsis thaliana* GRAS family transcription factor, that moves from the stele to cortical-endodermal tissue layers to specify cell fate and root patterning (***Nakajima et al., 2001***; ***Spiegelman et al., 2018***; ***Wu and Gallagher, 2013***, ***2014***). Other mobile factors with developmental importance include TARGET OF MONOPTEROS 7, PEAR transcription factors and miRNAs (***Lu et al., 2018***; ***Miyashima et al., 2019***; ***Skopelitis et al., 2018***).

Plant cells are connected by channels named plasmodesmata (PDs) that facilitate the transport of these molecules. PD are narrow membranous structures embedded in cell walls to allow for symplastic (cytoplasm-to-cytoplasm) molecular flux (***Figure 1***). The ER forms a tubular structure called desmotubule (DT) that traverses the PD, leaving a discrete cytoplasmic sleeve where molecular

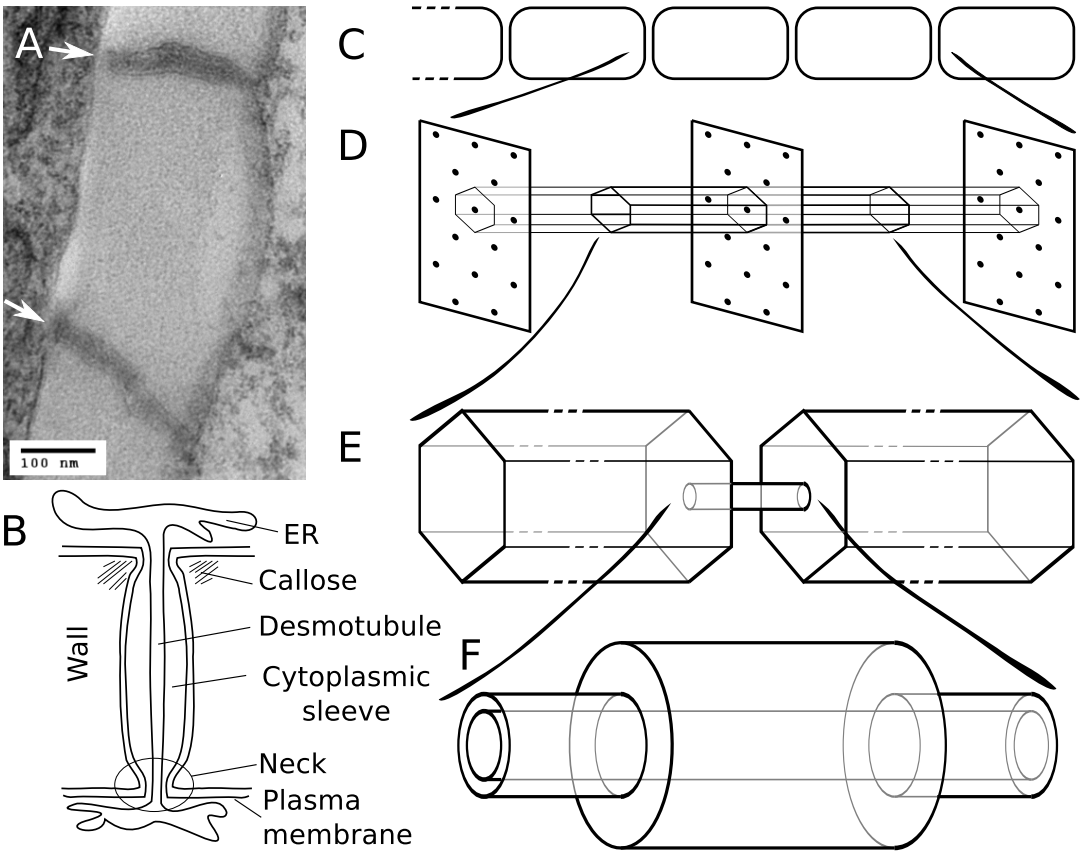

Figure 1. Modelling effective symplastic permeability: concept overview. A: Electron-microscopy picture showing two simple PDs (arrows) within cell walls of Arabidopsis cell culture. The image was kindly provided by Emmanuelle Bayer and Lysiane Brocard. B: Cartoon showing PD geometry and structural features. C-F: The model to determine effective symplastic permeability considers that connectivity within a cell file (C) is affected by the distribution of PDs in the cell wall (D) (modelled as a function of the cytoplasmic column belonging to a single PD (E)) as well as by the structural features of individual PDs (F).

transport occurs (***Nicolas et al., 2017a***; ***Sager and Lee, 2018***). The region closer to PD cytoplasmic apertures appears constricted (neck) in most tissue types although there are recent observations of 'straight' PDs in meristematic root sections(***Nicolas et al., 2017b***). Cell walls at PD locations play a key role in regulating its dimensions. The accumulation of callose, a cell wall beta-1,3 glucan polysaccharide synthesized by callose synthases and degraded by β-1,3-glucanases (***Zavaliev et al., 2011***; ***Amsbury et al., 2017***), is the best understood mechanism for the control of PD dimensions and symplastic transport capacity (i.e. effective symplastic permeability). Other factors such as membrane composition, shape and number of PDs change during development and between cell types adding extra dimensions to PD regulation (***Nicolas et al., 2017a***). Mutants blocked in PD form and function are embryo or seedling lethal, highlighting the importance of these structures for normal plant development (***Kim et al., 2002***; ***Benitez-Alfonso et al., 2009***; ***Xu et al., 2012***).

Small molecules can move via PD by diffusion (non-targeted transport). This is considered to be predominantly symmetrical (***Schönknecht et al., 2008***; ***Maule, 2008***), while in certain tissues, such as secreting trichomes (***Waigmann and Zambryski, 1995***; ***Gunning and Hughes, 1976***) and the phloem (***Ross-Elliott et al., 2017***; ***Comtet et al., 2017***), hydrodynamic flow may create directionality. The maximum size of molecules that can move by this generic "passive" pathway is often referred to as the "size exclusion limit" (SEL), which obviously depends on PD properties and structural features (***Dashevskaya et al., 2008***). Large molecules can move through PD via an "active" or "targeted" pathway overriding the defined SEL. This may involve additional factors that temporarily modify

these substrates, target them to the PDs, or induce transient modifications of the PDs to allow for the passage of larger molecules in a highly substrate dependent fashion (***Zambryski and Crawford, 2000***; ***Maule et al., 2011***).

Computational modelling approaches have been applied to model PD transport but, so far, these have mainly focused on hydrodynamic flow and the specific tissues where that matters (***Blake, 1978***; ***Jensen et al., 2012***; ***Ross-Elliott et al., 2017***; ***Comtet et al., 2017***). The few existing studies on diffusive transport do not consider neck constrictions or the approach of PDs from the cytoplasmic bulk. In the so-called "sub-nano channel model" (***Liesche and Schulz, 2013***) symplastic transport was modelled to be confined to nine cylindrical channels spanning the PD. This was based on a 9-fold rotational symmetry in enhanced "top view" electron micrographs but never validated experimentally in longitudinal sections. Instead, sparsely spaced axial spoke structures have been reported (***Ding et al., 1992***; ***Nicolas et al., 2017b***).

Experimental measurement of the parameters that determine effective symplastic permeability is difficult and many examples exist of misleading and/or conflicting results. Generally speaking two main approaches are used, providing results at different scales that are hard to reconcile. On the one hand, ultrastructural observations using transmission electron microscopy (EM) can provide useful data on PD dimensions and structural features but, despite recent advances, sample preparation affects the integrity and dimensions of PDs to an unknown extent potentially yielding an underestimation of relevant parameters (***Nicolas et al., 2017b***). On the other hand, tissue level measurement of symplastic fluxes is achieved using symplastic molecular reporters but this is limited to few molecular sizes, mostly fluorescein and its chemical relatives (hydrodynamic radii of about 0.4 to 0.6 nm) and GFP derived fluorescent proteins (such as DRONPA-s (28 kDa), Dendra2 (26 kDa) , (photoactive and non-photoactive) single GFP (27 kDa, hydrodynamic radius 2.45-2.82 nm) and its multiples (***Calvert et al., 2007***; ***Terry et al., 1995***; ***Chudakov et al., 2007***; ***Gerlitz et al., 2018***; ***Kim et al., 2005***; ***Rutschow et al., 2011***). Old data on symplastic permeability use either microinjection or particle bombardment with a wider range of dyes/ molecular reporters but these techniques can produce cellular stress, which affects PD function (***Liesche and Schulz, 2012***). Even when using the same dye/fluorescent molecule and the same tissue, these approaches produce very different outcomes, demonstrating that they are unreliable (e.g. see ***Haywood et al.*** (***2002***), or compare ***Rutschow et al.*** (***2011***) and ***Goodwin et al.*** (***1990***)). Less invasive methods involve the generation of transgenic lines expressing fluorescent proteins under specific cellular promoters (***Roberts et al., 2001***; ***Stadler et al., 2005a***) or photoactivation and photobleaching techniques (***Rutschow et al., 2011***; ***Gerlitz et al., 2018***) but these are time consuming and again limited to few molecular sizes.

In summary, despite recent advances in the development of probes and techniques, effective symplastic permeability is difficult to assess directly. The fast response of plants to wounding and other stresses, may render part of the ultrastructurally derived parameters less reliable than others, leading to apparently incompatible results when modelling diffusive symplastic transport (***Liesche and Schulz, 2013***). Ideally we would be able to integrate the results of these experimental approaches in a model that considers their limitations in order to get more accurate estimates of effective symplastic permeability and the underlying structural parameters. This brings us to our central question: what do we need to assume about PD size, number, structure, etc. to be able to reproduce tissue level measurements? PD geometry changes during development (***Roberts et al., 2001***; ***Fitzgibbon et al., 2013***), inspiring our second main question: how do distinct features of PD geometry influence transport properties?

Here, we describe the biophysical properties of diffusive symplastic transport considering detailed PD structural features (such as the DT and the neck region) and the approach from the cytoplasmic molecular bulk towards PDs that are either evenly distributed or clustered into pit fields (***Faulkner et al., 2008***) (***Figure 1***). Inside our model PDs, the entire cytoplasmic sleeve is available for particle diffusion ("unobstructed cytoplasmic sleeve model"). We investigate how neck/central region, wall thickness, the presence of a DT and PD clustering into pit fields affect

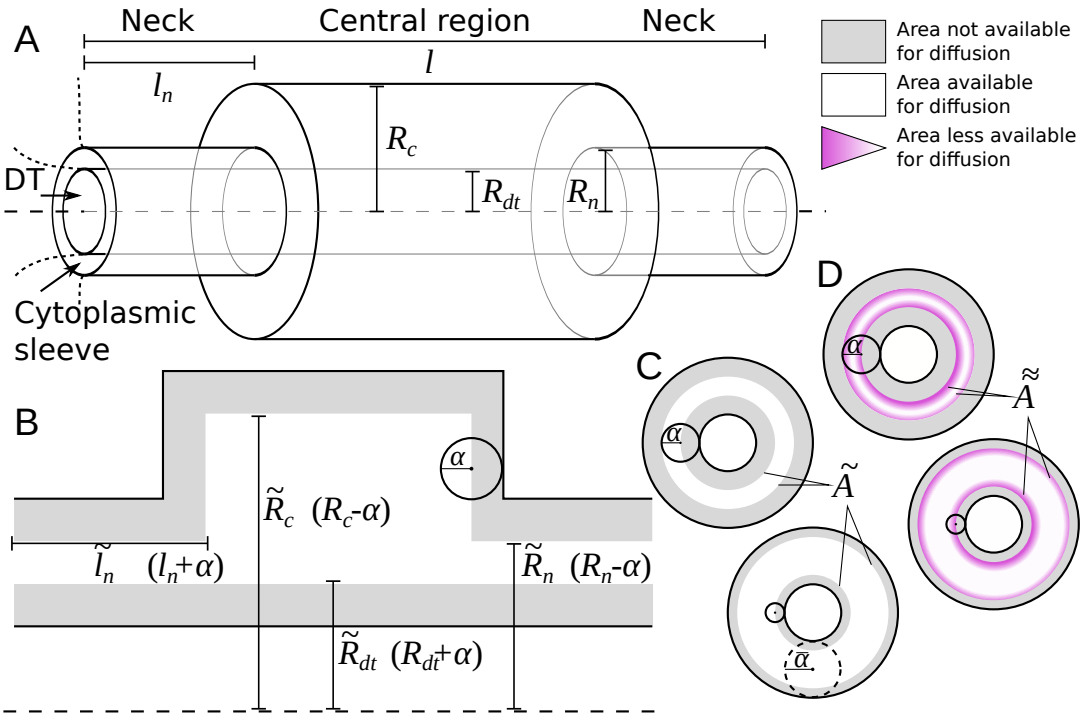

Figure 2. Model PD geometry and hindrance effects. A: Individual PDs are modelled using multiple cylinders with a total length l, neck (inner) radius R_n and neck length l_n, central region (inner) radius R_c and desmotubule (outer) radius R_{dt}. B,C: Illustration of the impact of steric hindrance and rescaled parameters. The gray areas of the longitudinal (B) and transverse (C) sections cannot be reached by the center of the particle with radius α (steric hindrance). For a concise description of the available volume and cross section area, we use the rescaled lengths $\tilde{l}_n = l_n + \alpha$, $\tilde{R}_c = R_c - \alpha$, $\tilde{R}_{dt} = R_{dt} + \alpha$ and $\tilde{R}_n = R_n - \alpha$. C: The cross section area available for diffusion on a transverse section was named $\tilde{A}$, which depends on the particle radius (α). $\tilde{A}$ is the area of the white ring in each cross section. The maximum particle size $\bar{\alpha}$ is illustrated with a dashed circle. For a particle of size $\alpha = \bar{\alpha}$, $\tilde{A} = 0$. D: In practice, particles spend less time diffusing close to the wall than farther away from it (hydrodynamic hindrance). Consequently, the area close to wall contributes less to diffusive transport, as illustrated with purple gradients. These additional hindrance effects are accounted for in $\tilde{\tilde{A}}$.

transport characteristics for different particle sizes, adding a functional context to some puzzling recent experimental observations. We also apply our framework to compute effective permeabilities for carboxyfluorescein (CF), a fluorescent dye used routinely to measure changes in symplastic permeability. Comparing calculated and experimentally measured values, we demonstrate that the relatively high effective CF permeabilities observed by (***Rutschow et al., 2011***) can be explained by our model of diffusive non-targeted symplastic transport and reveal the potential source of conflicts with ultrastructural measurements. We found that, in this context, our model performed better than the "sub-nano channel model" (***Liesche and Schulz, 2013***) referred to above. Our calculations demonstrate that multi-scale modelling approaches can integrate results from PD structural dimensions and molecular fluxes and reveal conflicts on these determinations. We, therefore, recommend these should be applied systematically when defining effective symplastic permeability for a particular tissue/molecule and/or biological context. To facilitate this, we share a python program for computing effective permeabilities from PD geometries as a community resource.

Results

Outline of the model

The problem of obtaining an effective wall permeability due to symplastic transport can be split in two parts: the movement through an individual channel representing a PD and the approach

to this channel from the cytoplasmic bulk (***Figure 1***). The basic geometrical terminology that we considered in our calculations is introduced in the cartoon PD shown in ***Figure 1***B. An overview of all mathematical symbols is given in ***Appendix 1***.

Obtaining good EM data of PD dimensions is notoriously hard. We therefore opted for the simplest possible geometrical description, with as few parameters as possible, that captures the essential spatial PD features (see methods). We modelled a single PD as a 3-part cylindrical channel (***Figure 2***A), with total length l, which would typically equal the local wall thickness. The ends of the channel were modelled by narrow cylinders representing the plasmodesmal "neck" constriction. These have length l_n and radius R_n. The central region has radius R_c. Over the whole length, the center of the channel is occupied by a "desmotubule" (DT) modelled as a cylinder of radius R_{dt}. The part available for diffusive transport, the cytoplasmic sleeve, is the space between the outer cylinder wall and the DT.

We made the arguably simplest choice of modelling particles as (non-additive, i.e. not interacting among themselves) hard spheres with radius α. This is partially supported by previous research showing that the hydrodynamic radius is the main determinant of PD transport characteristics, leaving behind, among others, particle charge (***Dashevskaya et al., 2008***; ***Terry and Robards, 1987***). We also assumed that PD walls are rigid, and hence are unable to deform to accommodate larger particles. These assumptions imply a boundary condition: the center of a particle cannot come closer to the wall than the particle's radius α (***Figure 2***B,C). This so-called steric hindrance reduces the volume that is available for diffusion of the particle's center in a size dependent manner. Moreover, the maximum particle radius that can pass the PD, $\bar{\alpha}$, is always well defined. In practice, a precise definition of the SEL in terms of molecule size/shape is hard to give, however, we can use $\bar{\alpha}$ to operationalize the SEL concept in a straightforward manner. To avoid confusion, however, we will consistently write $\bar{\alpha}$ when referring to our model.

We introduced rescaled geometrical parameters to account for the reduced available volume in a compact way: $\tilde{l}_n = l_n + \alpha$, $\tilde{R}_c = R_c - \alpha$, $\tilde{R}_{dt} = R_{dt} + \alpha$ and $\tilde{R}_n = R_n - \alpha$. With these, the available surface area (***Figure 2***C) is

$$\tilde{A}_x(\alpha) = \pi(\tilde{R}_x^2 - \tilde{R}_{dt}^2), \qquad (2\alpha < R_x - R_{dt}), \tag{1}$$

with $x = n$ for the neck and $x = c$ for the central region. In the typical situation that the neck is the narrowest part of the channel, the maximum particle radius that can pass is: $\bar{\alpha} = (R_n - R_{dt})/2$.

Assuming a homogeneous distribution of particle flux over (the available part of) each channel cross section, we can treat diffusion through the channel as a simple 1D problem. This way, the local concentration gradient at position x, ∇C_x, is inversely proportional to the available surface area A_x, so $\nabla C_c = \tilde{A}_n/\tilde{A}_c \nabla C_n$. The total concentration difference over the PD, $\Delta C = C_l - C_0$ is accordingly distributed over the channel: $\Delta C = 2\tilde{l}_n \nabla C_n + (l - 2\tilde{l}_n)\nabla C_c$. The steady state molar flow rate $Q(\alpha)$ through each channel is proportional to the entrance cross section: $Q(\alpha) = -D\tilde{A}_n \nabla C_n$, with D the particle's diffusion constant inside the PD. Solving these equations for ∇C_n leads to:

$$Q(\alpha) = -\frac{D\tilde{A}_n\tilde{A}_c}{2\tilde{l}_n\tilde{A}_c + (l - 2\tilde{l}_n)\tilde{A}_n}\Delta C. \tag{2}$$

This result can be improved further by incorporating hydrodynamic interactions between particles and walls (***Figure 2***D). To that end we employed the so-called hindrance factors $0 \leq H(\lambda) < 1$, which are based on proper cross sectional averaging of particle positions over time, as described by (***Dechadilok and Deen, 2006***). Based on geometrical considerations, we used the factors for a slit-pore geometry (see methods). These factors depend on the relative particle size λ. In our case, $\lambda = 2\alpha/(R_x - R_{dt})$. In the neck region, $\lambda = \alpha/\bar{\alpha}$. For the full expression and behaviour of $H(\lambda)$, see methods.

As $H(\lambda)$ already includes the effect of steric hindrance between wall and particle, we can adjust ***Equation 2*** by replacing every instance of $\tilde{A}_x$ with

$$\tilde{\tilde{A}}_x = H(\frac{2\alpha}{R_x - R_{dt}})A_x. \tag{3}$$

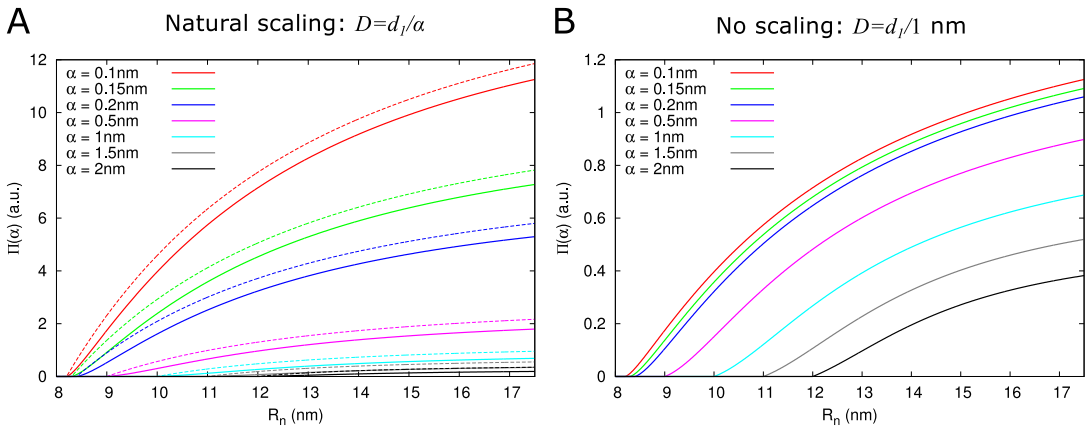

Figure 3. Impact of particle size (radius = α) on single pore effective permeability $\Pi(\alpha)$. A: Dependence of $\Pi(\alpha)$ on neck radius (R_n) and α (different line colours, see legend). The diffusion constant D is inversely proportional to particle size ($D = d_1/\alpha$). Dashed lines show $\Pi(\alpha)$ considering only steric hindrance, solid lines show full hindrance. B: Using the same diffusion constant for all particle sizes instead shows that the particle size dependence of $\Pi(\alpha)$ is largely due to the relation between particle size and diffusion constant. Parameters for calculations: $l = 200nm,\ l_n = 25nm,\ R_{dt} = 8nm,\ R_c = 17.5nm$. For simplicity we use inhomogeneity factor $f_{ih} = 1$ and $d_1 = 1nm^3/s$ in this figure. Therefore, permeabilities are in arbitrary units (a.u.).

Figure 3–Figure supplement 1. Impact of hindrance effects on $\Pi(\alpha)$.

For completeness, we note that the simplification of a uniform particle flux along the channel axis is violated near the neck-central region transitions, resulting in an error of a few percent (see methods for further discussion). We now define the permeation constant of a single PD, $\Pi(\alpha)$, through the rule steady-state flow rate = permeation constant × density jump, yielding

$$\Pi(\alpha) \equiv \frac{Q(\alpha)}{\Delta C} = \frac{D\tilde{\tilde{A}}_n\tilde{\tilde{A}}_c}{2\tilde{l}_n\tilde{\tilde{A}}_c + (l - 2\tilde{l}_n)\tilde{\tilde{A}}_n}. \tag{4}$$

We also defined τ as the corresponding estimate for the mean residence time (MRT) in the channel. Using a steady state mass balance argument this can be calculated as the number of particles in the channel divided by the number leaving (or entering) per unit of time (see methods for further description).

$$\tau(\alpha) = \int_0^l C_x\tilde{\tilde{A}}_x \mathrm{d}x/Q(\alpha) \tag{5}$$

Having defined the permeation constant of a single channel, the effective symplastic permeability of the wall as a whole ($P(\alpha)$, the quantity that can be estimated using tissue level measurements) follows from the definition $J = P\Delta C$ (steady state flux = permeability × density jump):

$$P(\alpha) = f_{ih}\rho\Pi(\alpha), \tag{6}$$

with ρ, the density of PDs per unit wall area (number/μm^2) and f_{ih}, a (density dependent) correction factor for the inhomogeneity of the wall ($0 < f_{ih} < 1$). The latter takes into account that the wall is, in fact, only permeable at discrete spots. To calculate f_{ih}, we considered a linear chain of cells of length L that are symplastically connected over their transverse walls (***Figure 1***B) and computed mean first passage times (MFPT) through a straight PD and a column of cytoplasm surrounding it, which we then converted to an effective wall permeability and compared the result with the uncorrected effected permeability computed using ***Equation 6*** for the corresponding PD geometry and $f_{ih} = 1$ (as described in the methods).

As expected, $P(\alpha)$ depends on particle size. Two factors underlie this size dependence, which both affect $\Pi(\alpha)$: hindrance effects, which reduce the space available for particle diffusion, and the fact that the diffusion constant is inversely proportional to particle size: $D = d_1/\alpha$. ***Figure 3***A and

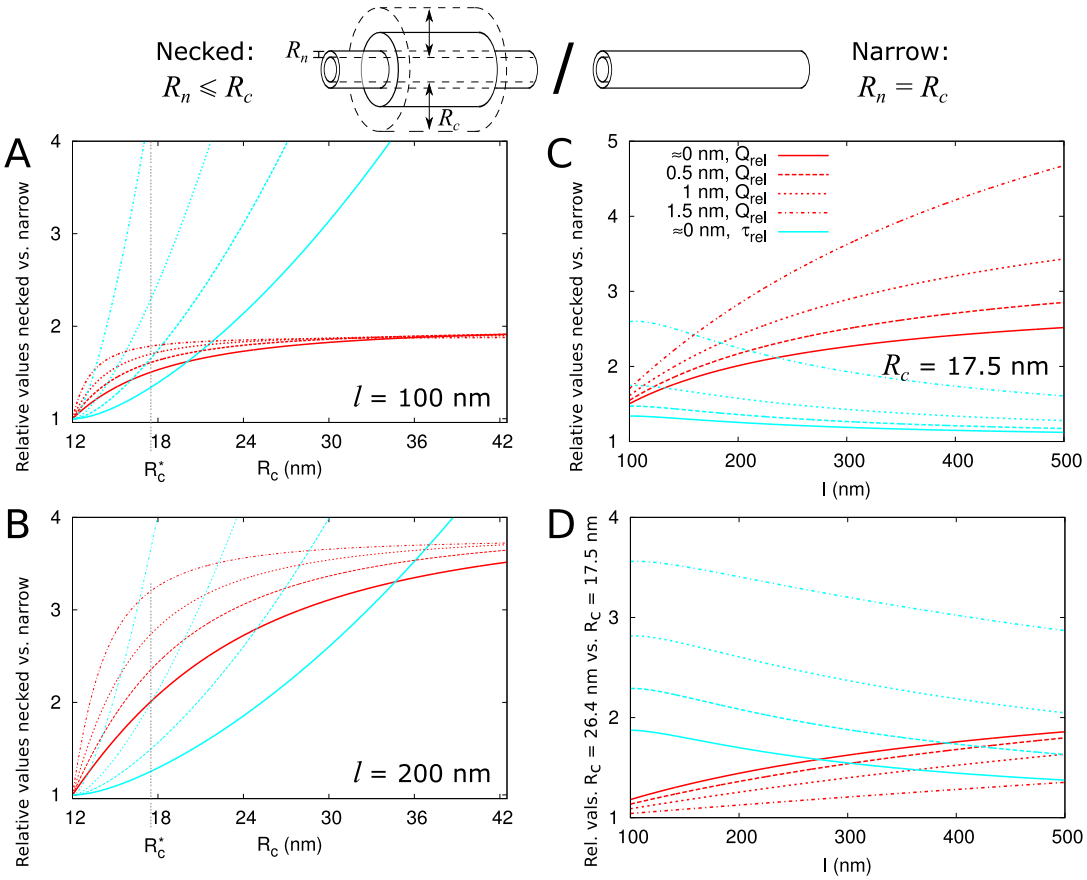

Figure 4. Impact of central region dilation on molar flow rate (Q) and mean residence time (τ). The same legend shown in C applies to all panels. A-C: red curves show the relation between molar flow rate in necked PD vs narrow PD $Q_{rel} = Q_{necked}(R_n, R_c)/Q_{narrow}(R_n)$ whereas cyan curves show the relation between mean residence time in necked PD vs narrow PD: $\tau_{rel} = \tau_{necked}(R_n, R_c)/\tau_{narrow}(R_n)$. Both quantities are computed for different particle sizes (solid: $\alpha \approx 0$, dashed: $\alpha = 0.5nm$, sparse dashed: $\alpha = 1nm$, dash-dotted: $\alpha = 1.5nm$). A,B: Q_{rel} and τ_{rel} are shown as a function of the radius in the central region R_c for different PD lengths (cell wall thickness) A: $l = 100nm$, B: $l = 200nm$. C: values calculated for $R_c = 17.5nm$ (R_c^* in A,B) as a function of PD length. D: Ratios of curves calculated for $R_c = 17.5nm$ (C) and $R_c = 26.4nm$ (***Figure 4–Figure Supplement 1***B) represented for varying PD lengths. Other parameters used for modelling are: $l_n = 25nm$, $R_n = 12nm$, $R_{dt} = 8nm$.

Figure 4–Figure supplement 1. Additional panels: $l = 500$ nm (similar to A,B), $R_c = 26.4$ nm (similar to C).

Figure 3–Figure Supplement 1 show that hindrance effects have the strongest impact for particle sizes close to the maximum $\bar{\alpha}$, whereas the particle diffusion constant always has a large impact ***Figure 3***B.

Using the model presented here, we computed the effects of different PD structural features and changes in PD density and distribution on effective symplastic permeability and its dependence on particle size as described below.

"Necked" PDs increase molecular flux in thicker cell walls

Evidence suggests that PDs often have a neck region of reduced radius in comparison to the central region. We investigated how a constricted neck region, or, similarly, a dilated central region, affects PD transport. For this, we compared transport properties while conserving the size selectivity (constant $\bar{\alpha}$). We investigated how both the transport volume (using ***Equation 2***) and transport time (τ as above) change when the central region is dilated. To compare channels with neck and dilated central region ($R_n \leq R_c$) with narrow straight channels ($R_n = R_c$), we define a relative molar flow rate as $Q_{rel} = Q_{necked}/Q_{narrow}$ and similarly relative τ_{rel} (***Figure 4***). For a more detailed discussion of τ_{rel}

and its computation, see methods and ***Appendix 2***.

We then investigated how both Q_{rel} and τ_{rel} change with increasing central region radius R_c and how this depends on particle radius α and PD length l (***Figure 4***). The panels A and B show that molar flow rate increases with the central radius but quickly saturates, whereas mean resident time increases much faster and runs off the graph. Moreover, both quantities increase faster for larger particle sizes (α, dashed lines). In fact, from studying the limiting behaviour of the underlying formulas, we found that Q_{rel} is always less than its theoretical maximum $\frac{l}{2\tilde{l}_n}$, whereas τ_{rel} ultimately scales quadratically with R_c, and, equivalently, linearly with the surface ratio $\tilde{\tilde{A}}_c/\tilde{\tilde{A}}_n$ (see ***Appendix 3*** and ***Appendix 3 Figure 1***). In simpler terms: the benefits of increased transport volume with increasing R_c saturate, and instead the costs in transport time increases ever faster with further dilation of the central region. This defines a trade-off between transport volume and transport time with increasing R_c when we analyze a single PD with a given entrance area.

Our computations also show that with increasing PD length l, the balance between both factors shift, because a much larger increase of Q_{rel} is possible (***Figure 4***A-C). This suggests that dilation of the central region is more favourable in thicker cell walls. Interestingly, this theoretical observation correlates well with a recent EM study in *Arabidopsis* root tips (***Nicolas et al., 2017b***). The authors observed that PDs with a distinct dilated central region and neck region occurred mostly in thicker cell walls (average 200 nm), whereas in thin cell walls (average 100 nm), they found mostly straight PDs.

Additionally, ***Nicolas et al.*** (***2017b***) observed a smaller and less variable radius in channels where the central region was occupied by spokes compared to channels without them (R_c= 17.6 nm vs. 26.4 nm on average). To analyze the effects of these changes on molar flow rate and MRT, we redrew the curves to compute relative values for R_c=26.4 nm and R_c= 17.5 nm as a function of PD length (cell wall thickness) and for various particle sizes. As an example, panel C shows the variations observed when considering R_c= 17.5 nm (R_c^* in A,B). We found that the molar flow rate Q_{rel} increases less than the MRT τ_{rel} when increasing R_c from 17.5 nm to 26.4 nm, except for the smallest particle sizes in combination with large l (***Figure 4***D). This data suggests that in cell walls of moderate thickness, it performs better to restrict the radius of the central region.

In summary, for a given particle, transport time and transport volume scale differently with the radius of the central region thus producing necked PDs with a dilated central region becomes more favourable when cell wall thickness increases. However, if the radius of the central region becomes too wide (as exemplified here for R_c 26.4 nm) the increase in transport volume does not compensates for the delay in transport time. Interpretation of this result might explain why mostly straight PDs are found in recently divided cells (with thin cell walls) and why spokes (potentially limiting the radius of the central region) are often observed in mature PDs.

The desmotubule increases PD transport and changes the dependence on particle size

A conserved feature of PDs –at least in embryophytes– is the presence of the DT, so we asked how this structure affects the transport capacity for particles of various sizes. In our model, the DT and the neck radius jointly define the maximum particle radius $\bar{\alpha}$. Assuming that size selectivity and net flux are under selection, we estimated the number of cylindrical channels required to match a single PD with DT. Using that $P(\alpha)$ is proportional to orifice area ($\approx A_n$), we first computed $n_c(\bar{\alpha})$, the number of circular channels that would offer the same A_n as a single channel with a DT of radius $R_{dt} = 8nm$ and the same $\bar{\alpha}$ (see methods):

$$n_c(\bar{\alpha}) = \frac{(R_{dt} + 2\bar{\alpha})^2 - R_{dt}^2}{\bar{\alpha}^2} = 4\frac{R_{dt} + \bar{\alpha}}{\bar{\alpha}}. \quad (7)$$

Figure 5A displays the $n_c(\bar{\alpha})$ as a function of the maximum particle size. As an example, when $\bar{\alpha} = 2nm$, 20 cylindrical channels without DT would be needed to match the orifice surface area of a single channel with DT (with $R_{dt} = 8nm$). This number decreases for larger $\bar{\alpha}$. We then considered

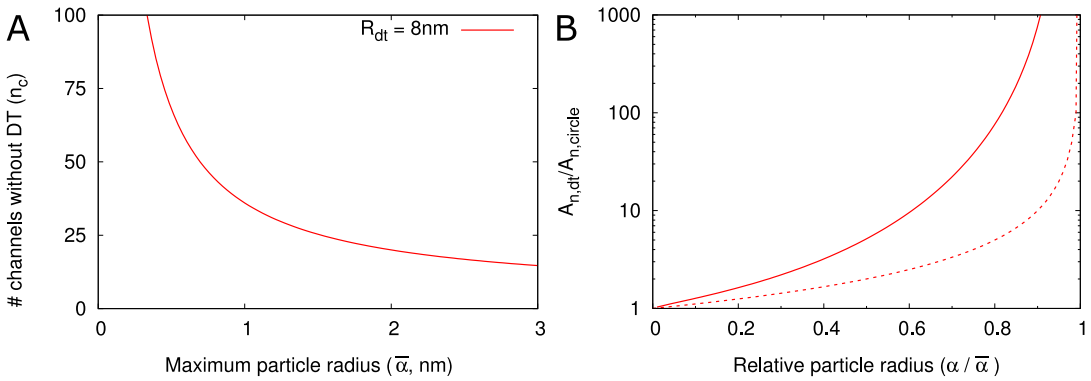

Figure 5. DT increases the cross section surface area available for transport per channel given a maximum particle radius $\bar{\alpha}$. A: The number of cylindrical channels (n_c) that is required to match the total entrance surface of a single channel with $R_{dt} = 8nm$ and the same maximum particle radius $\bar{\alpha}$. B: shows the relative area available for transport (A_n) in relation to relative particle size ($\alpha/\bar{\alpha}$) when comparing channels with DT and the equivalent number of cylindrical channels. Total surface area is the same. Solid lines include all hindrance effects ($\tilde{\tilde{A}}_{n,dt}/\tilde{\tilde{A}}_{n,circle}$; cf. ***Figure 2***D). Dashed lines includes steric effects only ($\tilde{A}_{n,dt}/\tilde{A}_{n,circle}$; cf. ***Figure 2***C).

Figure 5–Figure supplement 1. Hindrance factors with and without DT.

that not all of this surface area is available for transport because of hindrance effects (***Figure 2***B-D). We found that even if the total surface area is the same, the channel with DT has a larger available surface area than the equivalent number of cylindrical channels. This is because in cylinders a larger fraction of the surface is close to the wall and, hence, hindrance effects are much more severe (***Figure 5***B, ***Figure 5–Figure Supplement 1***). The difference increases with increasing relative particle size ($\alpha/\bar{\alpha}$). Steric hindrance, i.e. the center of a hard particle cannot come closer to the wall than its own radius, plays only a minor part in this effect (***Figure 5***B).

Clustering of PDs in pit fields reduces effective symplastic permeability

The cell wall is only permeable for symplastic transport where the PDs are. In this scenario, particles have to diffuse longer distances (on average) to reach a spot to cross the wall compared to a wall that is permeable everywhere. To account for this, we have introduced a correction factor, or "inhomogeneity factor", f_{ih} in ***Equation 6*** for the effective symplastic permeability. Here, we explore how f_{ih} depends on all model parameters. To calculate f_{ih}, we treated the cytoplasm as a homogeneous medium. This simplifying assumption is necessitated by the lack of detailed information on the cytoplasm structure and how it differs among cells. Effectively, we assumed that the obstructing effects of ER, vacuoles, etc. are similar throughout the whole cell volume and thus can be captured in a single reduced cytoplasmic diffusion constant.

First, we calculated f_{ih} for isolated PDs positioned on a triangular grid in the cell wall (***Figure 6***A), as described in the methods. In ***Figure 6*** we presented f_{ih} as a function of R_n and explored its dependence on particle size α (***Figure 6–Figure Supplement 1***A), presence/absence of DT (***Figure 6–Figure Supplement 1***A), cell length L (***Figure 6–Figure Supplement 1***B), density of PD ρ (B), wall thickness l (C) and PD distribution in the wall (D). We found that, provided that R_n is large enough for particles to enter (as indicated by vertical cyan lines in ***Figure 6–Figure Supplement 1***A), f_{ih} is independent of cell length L and particle size α (***Figure 6–Figure Supplement 1***A,B) and is not affected by the DT. We also adjusted the computation for different regular trap distributions (***Berezhkovskii et al., 2006***) to find that f_{ih} also hardly depends on the precise layout of PDs (***Figure 6***D). Although variations in f_{ih} appear larger at low PD densities, for typical R_n values (for example 17.5 nm as in Figure 4) density only has a minor impact (***Figure 6***B). Finally, we found an increase of f_{ih} with increasing PD length l, saturating to its theoretical maximum of $f_{ih} = 1$ in thick cell walls (l> 500nm) (***Figure 6***C). This result reflects the increasing time required for passing the PD itself with increasing PD length and, hence, a decreasing relative importance of the cytoplasmic

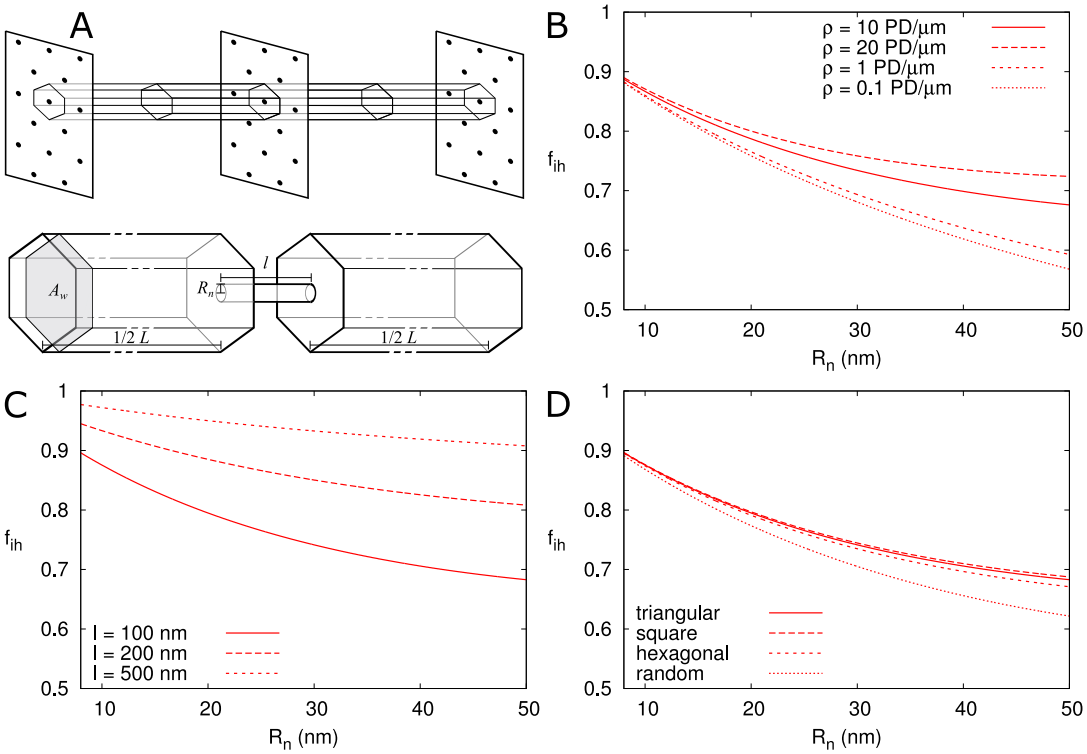

Figure 6. Correction factor f_{ih} for inhomogeneous wall permeability depends on PD distribution, cell wall thickness and neck radius. A: The cartoon shows the geometrical considerations and parameters used to model the diffusion towards PDs. Cell wall inhomogeneity is incorporated as a correction factor f_{ih}, $0 < f_{ih} \leq 1$, which measures the relative impact of cytoplasmic diffusion towards the locations of the PDs in the cell wall compared to reaching a wall that is weakly but homogeneously permeable (i.e., with $f_{ih} = 1$). The cytoplasm is considered homogeneous. Each bit of cytoplasm can be assigned to the PD closest to it. With PDs on a regular triangular grid, the cytoplasm belonging to a single PD, with an outer (neck) radius R_n, is a hexagonal column with cross section area Aw and 1/2 of the cell length L on either side of the wall. B-D: f_{ih} is represented as a function of R_n, calculated for PDs without DT. In all cases, solid lines correspond to: $l = 100$nm, $L = 10\mu$m, $\alpha = 0.5$nm, a PD density of $\rho = 10$ PD/μm^2, and PDs distributed on a triangular grid. Broken lines show the effects of changes in PD density ρ (B), PD length l (C) and PD distribution (D).

Figure 6–Figure supplement 1. f_{ih} is not affected by particle size α, presence of DT, or cell length L

diffusion.

Second, we investigated the effect of PDs grouped in small clusters resembling pit fields (see methods). The average centre-to-centre distance between PDs in pit fields considerably varies across species, with reported / calculated distances between 60 and 180 nm (***Terauchi et al., 2015***; ***Schmitz and Kühn, 1982***; ***Danila et al., 2016***; ***Faulkner et al., 2008***). The lowest values, however, are from brown algae, which have a different PD structure from higher plants (***Terauchi et al., 2012***). As a default, we used $d = 120$ nm, which also coincides with measurements on electron micrographs of tobacco trichomes presented in (***Faulkner et al., 2008***).In ***Figure 7***A we calculated f_{ih} as a function of total PDs ("entrances") per area of cell wall for different numbers of PDs p clustered in a single pit field. We found that f_{ih} decreases with increasing number of PDs in a pit. When the total number of PD per square area is the same, the distance between pits must increase with the number of PD clustered in one pit, which explains the reduction in f_{ih} (more "inhomogeneous" cell walls). Different from isolated PDs, ***Figure 7***A also reveals that, when grouped in pit fields, there is a strong dependence of f_{ih} on total PD density (number of PD entrances per area of cell wall). This could be predicted from ***Figure 6***B for isolated PDs, where density dependence also increases with increasing PD radius, because cluster radii R_{pit} are even larger than 50 nm. ***Figure 7***B shows that clustering (in this case 7 PDs) increases the dependence of f_{ih} on PD length (compare solid and dashed lines of the same colour). Increasing the distance between PDs within the cluster (***Figure 7***C), also increases the dependence of f_{ih} on PD density. As the distance between PDs in the cluster increases, the PD density *within* the cluster decreases. The different arrangements of PDs in the small model clusters also causes differences in *within cluster* PD density. Also in this case, we observe the steepest dependency of f_{ih} on ρ for the clusters with the lowest *within cluster* PD density (particularly $p = 5$, 6 and 19: indicated with blue lines in ***Figure 7***A; see also ***Table 2***).

It is hypothesized that PD clustering arise or increases in the process of increasing PD number post cytokinesis, possibly through (repeated) "twinning" of existing PDs (***Faulkner et al., 2008***). We, therefore, also investigated the effect of increasing the number of PDs per cluster (p), starting from 1 PD per cluster (***Figure 7***D). As expected, $P(\alpha)$ always increased with the increase in cluster size/PD number (***Figure 7***D), despite the decrease in f_{ih} compared to homogeneously distributed PDs. This increase was larger for larger pit densities (number of pit fields per cell wall area).

In summary, for isolated and roughly evenly distributed PDs, the correction factor f_{ih} for inhomogeneous wall permeability has only a minor role on $P(\alpha)$. For realistic PD dimensions (R_n <20-25 nm), only PD length l seems to matter to a degree that might be experimentally measurable. However, when considering clusters of PDs, as is common in pit fields, f_{ih} is markedly reduced, and PD length and density have a much larger impact on f_{ih}. We observed the biggest difference between isolated PDs and pairs, i.e., when going from single to twinned PDs (***Figure 7***A).

Application of the model to compute effective permeability for fluorescein derivatives

In a system where non-targeted symplastic transport is fully driven by diffusion (so no (significant) active transport or hydrodynamic flow), our calculations using reasonable PD dimensions and densities should yield values close to the ones measured experimentally. As a resource to test this hypothesis, we have build a Python program, PDinsight, that computes effective permeabilities from parameter measurements extracted from EM. As some of these parameters might be more reliable than others, we also created a mode in the program to predict what are the minimum requirements in terms of parameter (combination of parameters) values to obtain experimentally measured symplastic permeability. Exploring these requirements is equivalent to testing hypotheses like: "What if PD aperture is larger than observed with EM? or if the molecular radius is smaller than predicted?". Predictions made with the program can be used to explain experimental results, highlight areas/parameters that need more investigation and can help with the design of new strategies to change effective symplastic permeability in vivo. For a full description of the program and its possibilities, see ***Appendix 6***.

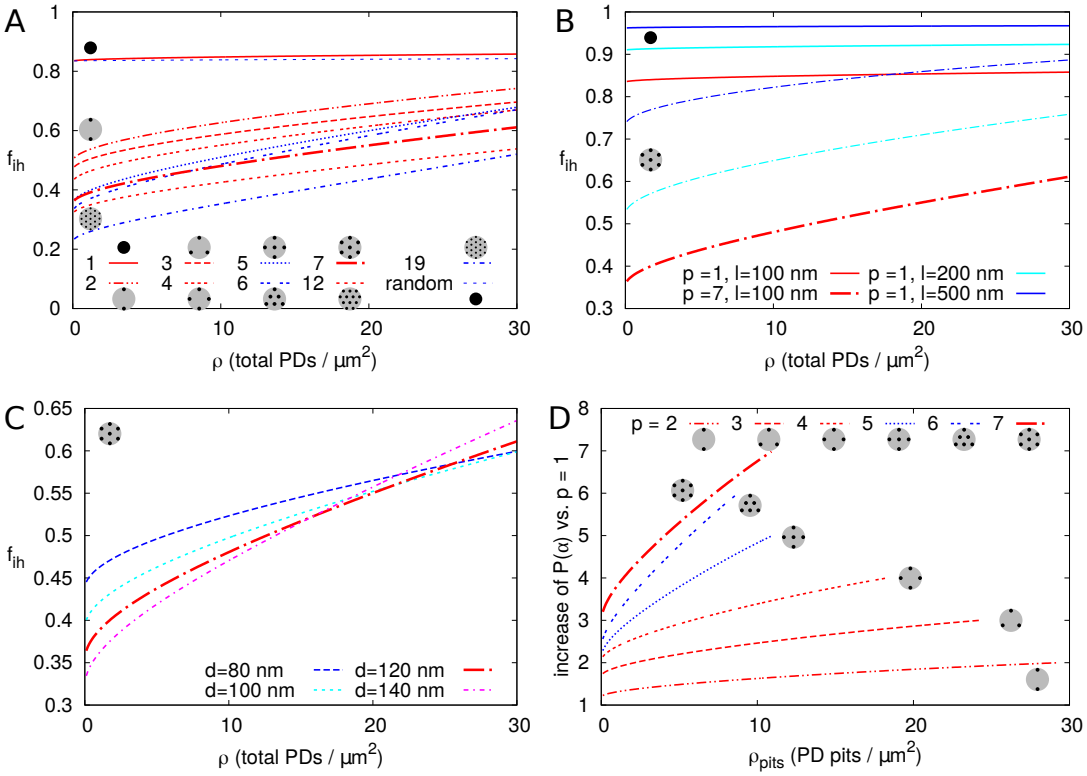

Figure 7. Impact of PD clustering into pit fields. PD organization within pits is indicated with small cartoons in each graph. Pits themselves are distributed on a regular triangular grid. A-C: f_{ih} is represented as a function of total PD density ρ (the total number of PD entrances per unit of cell wall area) for: a varying number of PDs per cluster p (as indicated by line type, A), for different PD length l (B, solid lines: isolated PDs, dash-dotted lines: 7 PDs per cluster, red colour indicates l: 100 nm, cyan for 200 nm, blue for 500 nm) and for different PD spacing within clusters (C, shown for clusters of 7 PDs with centre-to-centre distance d as indicated by line type and colour). Cluster sizes 5, 6, and 19 are indicated with blue lines for readability (A,D). For comparison, f_{ih} for non-clustered but randomly distributed PDs is also indicated. D: The impact of increasing the number of PDs per cluster p on $P(\alpha)$ as a function of cluster density ρ_{pits} (the number of pit fields per unit of cell wall area). Lines show the fold increase of $P(\alpha)$ when increasing the number of PDs per cluster from 1 to the number indicated by the line type (same as in A). Lines are terminated where f_{ih} of clusters meets f_{ih} of isolated PDs at the same total PD density. Beyond that, calculation results are no longer reliable because clusters get too close and the impact of clustering on f_{ih} could be considered negligible. A-D: Default parameters: $l = 100$ nm, $d = 120$ nm, $R_n = 12$ nm.

As a test case, we used the model to explain the permeability measurements in *Arabidopsis thaliana* roots reported for carboxyfluorescein (CF) diacetate: a membrane permeable non-fluorescent dye that once converted inside cells into a fluorescent version of fluorescein can only move from cell to cell via the PDs (**Rutschow et al.** (**2011**)). Using a technique named fluorescence recovery after photobleaching (FRAP), CF effective permeability in transverse walls in the root meristem zone (measured $\approx 200\mu m$ from the quiescent centre) was estimated to be 6-8.5 $\mu m/s$.

PD densities in transverse walls of *Arabidopsis thaliana* roots were reported by (**Zhu et al., 1998**). Fluorescein has a Stokes radius of approximately 0.5 nm (**Champion et al., 1995**; **Corti et al., 2008**) and a cytoplasmic diffusion constant of $D = 162\mu m^2/s$ (one third of its water value) (**Rutschow et al., 2011**). Feeding these numbers to the model, and considering that PD appears as straight channels in these walls (**Nicolas et al., 2017b**), we are able to reproduce the measured permeability values for observed PD densities **Zhu et al.** (**1998**) only if we assume a relatively wide open neck ($R_n > 14.8nm$) (**Figure 8**A,B, **Table 1**). This prediction is plausible if we consider that, in the same tissues, GFP (a protein with a reported hydrodynamic radius of 2.45 nm (**Calvert et al., 2007**) to 2.82 nm (**Terry et al., 1995**)) moves intercellularly (**Stadler et al., 2005b**). Using our default R_{dt}, R_n is predicted to be distinctly wider than 13-14 nm for GFP to move. We also explored the possibility that PD densities are higher than determined by (**Zhu et al., 1998**). We found that to obtain the required effective permeabilities for CF with our default $R_n = 12$ nm, we would need PD densities of 33 - 47 PDs μm^{-2} (**Table 1**).

Using the model, we also explored the effect of 'necked' PDs by adding a wider central region to PDs. For a central radius $R_c = 17.6\ nm$, the required R_n to reproduce CF permeability values would decrease by perhaps 1 nm or at most 3 nm (for $R_c = 26.4\ nm$) considering a PD density in the order of $\rho = 10\mu m^{-2}$ (**Figure 8**C, R_c values from (**Nicolas et al., 2017b**)). In thicker cell walls (**Figure 8**D), the calculated effective permeabilities remained low suggesting no effective gain from increasing cavity radius (see also **Figure 4**).

Rutschow *et al.* also reported drastic changes in effective permeability after H_2O_2 treatment. They found a strong decrease in symplastic permeability to $\approx 1\mu m/s$ after treatment with a "high" H_2O_2 concentration, which was explained by rapid PD closure through callose deposition. Using our program we found that, for this reduction of $P(CF)$, callose must reduce R_n to 11 nm ($\rho = 10\mu m^{-2}$) or 10.6 nm ($\rho = 13\mu m^{-2}$), resulting in $\bar{\alpha}$ = 1.5 nm or 1.3 nm, respectively. The authors also found a strong increase in permeability to $\approx 25\mu m/s$ after treatment with a "low" H_2O_2 concentration. Reproducing this increase would require a large increase of R_n to approximately 29 nm for $\rho = 10\mu m^{-2}$ (**Figure 8**A,B, **Table 1**B). Alternatively, without change in R_n, a slightly more than 4 fold increase in PD density would be required to reproduce this high effective permeability (**Figure 8**B, **Table 1**C). The increases in $P(\alpha)$ that could be obtained through DT removal were by far insufficient to explain the reported effect of mild H_2O_2 treatment (**Figure 8**C,D), making DT modification or removal an unlikely explanation for this change.

Taken together, these calculations indicate that our model for diffusive symplastic transport can indeed explain experimentally observed measurements of effective symplastic permeability, but only with somewhat wider PDs/neck regions than expected yet in line with the observed permeability for GFP and within the range of PD diameters measured in thick cell walls. Alternatively, similar changes in symplastic permeability can be achieved with several fold higher densities than typically measured. These predictions provide a framework for experimental validation. We also compared the results obtained with our model and the sub-nano channel model reported before (**Liesche and Schulz, 2013**). Using the sub-nanochannel model much larger PD densities would be required to achieve the same $P(CF)$: roughly twice as large for $\bar{\alpha}$ = 3.5-4 nm and even larger for smaller $\bar{\alpha}$ (see **Appendix 5**A). These results favour our model for offering more plausible hypotheses to explain the experimental results for CF and the impact of H_2O_2 treatment on effective permeability.

Table 1. Parameter requirements for reproducing measured $P(CF)$ values with the default model. This table was generated using PDinsight. A: Required density (ρ) for a given $\bar{\alpha}$ and neck radius (R_n). B: Required $\bar{\alpha}$ and corresponding R_n for a given ρ. C: values required to reproduce $P(CF) = 25\mu$m/s. Values computed for a 2x, 3x and 4x increase of ρ are also shown. This is done both for a uniform increase of the density ($p = 1$) and for (repeated) twinning ($p > 1$) from a uniform starting density (indicated in bold). p is the number of PDs per pit.

A $P(CF)$(μm/s)	$\bar{\alpha}$ (nm)	R_n (nm)	ρ (PD/μm^2)
6	2.0	12	33.5
	2.5	13	22.7
	3.0	14	16.8
	3.4	14.8	13.8
	3.5	15+	13.2
	4.0	16+	10.7
8.5	2.0	12	47.2
	2.5	13	32.0
	3.0	14	23.7
	3.4	14.8	19.4
	3.5	15+	18.5
	4.0	16+	15.0

B $P(CF)$(μm/s)	ρ	$\bar{\alpha}$	R_n (nm)
6	10	4.2	16.3
	13	3.5	15.1
8.5	10	5.2	18.4
	13	4.4	16.8
1	10	1.5	11.0
	13	1.3	10.6

C $P(CF)$(μm/s)	ρ	p	$\bar{\alpha}$	R_n (nm)
25	**10**	**1**	**10.5**	**28.9**
	20	1	6.6	21.2
		2	7.2	22.5
	30	1	5.1	18.1
		3	5.6	19.2
	40	1	4.2	16.4
		4	4.6	17.2
	13	**1**	**8.8**	**25.6**
	26	1	5.6	19.1
		2	6.0	20.0
	39	1	4.3	16.6
		3	4.6	17.2
	52	1	3.6	15.1
		4	3.8	15.5

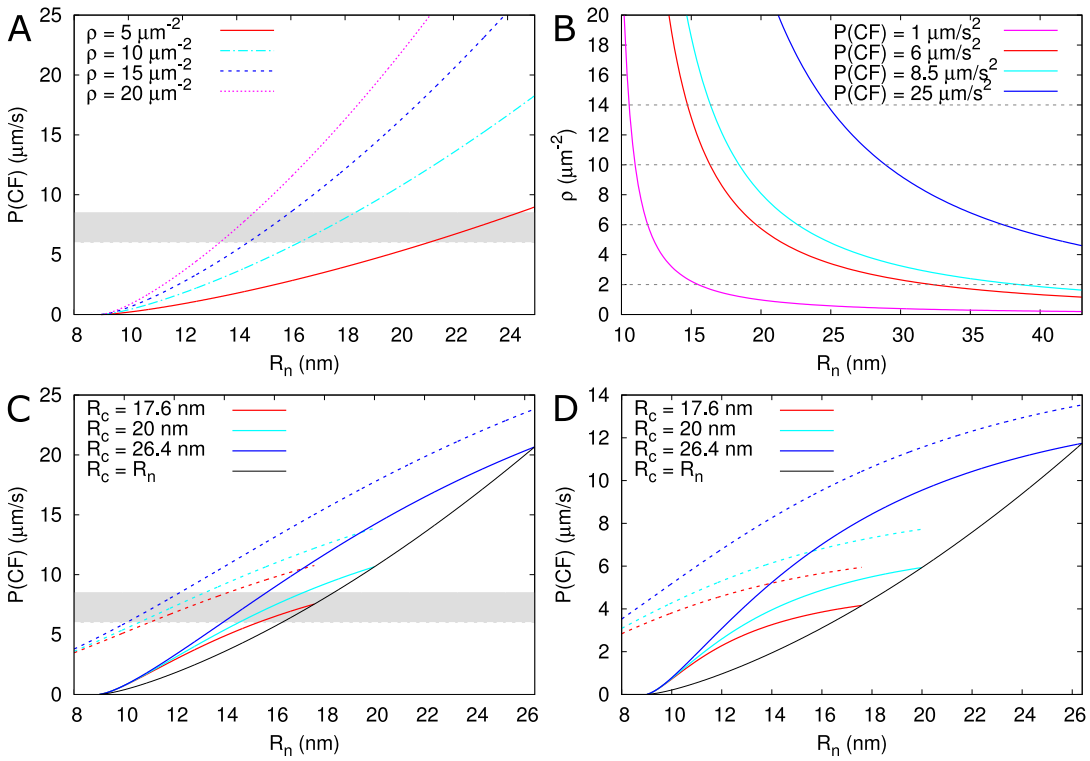

Figure 8. Calculated effective permeabilities for carboxyfluorescein (CF) as a function of PD aperture at the neck R_n. A,B: shows the graphs for straight channels. A: effective permeabilities are calculated for different PD densities (different colour curves). The horizontal gray band in A and C indicates the cortical values observed by ***Rutschow et al.*** (***2011***). B: shows the PD density required to obtain measured values of $P(CF)$ (different colour curves) as a function of R_n. Horizontal broken lines are introduced to aid readability. C,D: shows that effective permeability increases in necked PDs ($R_c > R_n$). As a reference, values for straight channels are indicated in black. Dashed curves show values calculated for channels without DT. D: shows the same calculations as C but for longer PDs $l = 200\ nm$. Default parameters: $\alpha = 0.5\ nm$, $D = 162\ \mu m^2/s$, $l_n = 25\ nm$, $l = 100\ nm$, $R_{dt} = 8\ nm$, $\rho = 10\ \mathrm{PD}/\mu m^2$, PDs are spaced on a triangular grid, without clustering.

Discussion

In this manuscript, we presented a method for calculating effective wall permeabilities for non-targeted, diffusive symplastic transport based on the dimensions and distribution of PDs and on the size of the mobile particles. For individual PDs, we used a minimal geometrical description that allowed us to extensively investigate the effects of constrictions in the PD neck region and the implications of a DT at the PD axis on transport properties. Because PDs are narrow, our calculated effective symplastic permeabilities were heavily affected by molecular hindrance effects. To assess the impact on effective symplastic permeability of various PD distributions, including clustering into pit fields, we introduced the inhomogeneity factor f_{ih} that accounts for the fact that the wall is only permeable at certain spots (where the PDs are located). Clustering into pit fields had by far the largest impact on this factor, particularly for lower PD densities. This means that not only total PD density, but also the degree of clustering is important information for calculating effective wall permeability from experimental data. We applied our model to calculate the effective permeability for fluorescein in transverse walls of Arabidopsis root cells. Assuming purely diffusive transport and parameters based on various ultrastructural measurements, we were able to reproduce the observed effective permeabilities for CF and to assess the plausibility of different hypotheses aimed at resolving the conundrum of apparently incompatible measurements at different scales. These predictions could be further constrained by a consistent set of both ultrastructural and functional measurements of the same tissue/ developmental stage, with identical experimental conditions.

In our model, the DT gives the PD an annular cross section, which strongly increases transport capacity compared to cylindrical entrances, particularly for relatively large molecules. In essence, the difference between annular and cylindrical channels explains why our unobstructed sleeve model performs better in explaining measured CF permeabilities (***Rutschow et al., 2011***) than the sub-nano channel model described by others (***Liesche and Schulz, 2013***). Having a DT offers an additional flexibility in regulating size selectivity through the possibility of a dilated state of the PD by displacement or temporal removal of the DT (***Zambryski and Crawford, 2000***; ***Crawford and Zambryski, 2000***). This feature, however, can be exploited for the spreading of viruses (***Benitez-Alfonso et al., 2010***) and other intracellular parasites such as the fungus *Magnaporthe oryzae* (***Kankanala et al., 2007***). Functional PDs without DT (and inner diameter of 10-20 nm) have been reported for the brown algae species *Dictyota dichotoma* (***Terauchi et al., 2012***). Due to their very high membrane curvature, DT formation requires curvature-inducing proteins (such as reticulons) and a special lipid composition (***Tilsner et al., 2011***; ***Grison et al., 2015***; ***Knox et al., 2015***). It is likely that performance benefits of the DT offset these costs and disadvantages and it is therefore under evolutionary selection. The shape of ER structures near PD entrances could also have an effect and would be an interesting topic to consider for future investigations.

We have also calculated the performance costs (transport rate) and benefits (transport volume per PD) of having distinct central and neck regions. Whereas the transport time scales quadratically with the radius of the central region (R_c), the transport volume has a strong upper bound that increases with channel length. These results suggest that straight PDs perform better in thin (average 100 nm) cell walls and necked PDs in thick (average 200 nm) cell walls, which correlates with recent observations (***Nicolas et al., 2017b***). This is not, however, the only way to explain these observations. Necked PDs might appear because 1) size selectivity is more efficient controlled by restricting callose deposition to a 20-30 nm long neck region, 2) the formation of "spokes" in the central region lead to this structural modification, and/or 3) the material properties of cellulosic cell walls and PD cell membranes only allow for a distinctly wider central region if the channel is long enough.

In our model, we naturally define the SEL as $\bar{\alpha}$, the maximum particle radius that could fit through the model PD, but experimental determination of this value is difficult and often relies on the transport of detectable, typically fluorescent, molecules such as CF. The limited set of suitable molecules introduces a large uncertainty in SEL measurements and hence $\bar{\alpha}$. Also other biological factors could lead to an underestimation as well as an overestimation of $\bar{\alpha}$. For example, sucrose moves symplastically from bundle sheet cells (BSC) to intermediary cells (IC), where it is polymerized into the larger oligomers raffinose and stachyose, that do not diffuse back in detectable amounts (***Haritatos et al., 1996***; ***Liesche and Patrick, 2017***). Two explanations have been suggested: 1) a discriminating PD SEL at this interface, which prevents the back transport of raffinose and stachyose ***Liesche and Schulz*** (***2013***), or 2) open PDs combined with a directional flow which could be sustained by the xylem flow ***Comtet et al.*** (***2017***). Only the latter can explain the observed amount of sucrose transport ***Liesche and Schulz*** (***2013***); ***Comtet et al.*** (***2017***). A directional flow would also explain the observation that PD length in this system does not correlate with transport capacity ***Liesche et al.*** (***2019***). This example illustrates that overlooking a symplastic flow could largely affect calculated permeabilities.

An overestimation of $\bar{\alpha}$ could occur for non-spherical molecules or temporal variations in PD properties. Although a molecule's hydrodynamic radius is a better predictor of its symplastic transport efficiency than its molecular weight (***Terry and Robards, 1987***; ***Dashevskaya et al., 2008***), it conceptually assumes a static replacement sphere. Molecules may be more flexible and/or have a shortest dimension than what is captured by its diffusive behaviour in bulk. PDs might also accommodate molecules that are larger than expected, either through interactions with specific PD proteins (***Benitez-Alfonso et al., 2010***) or because membranes and/or cell wall domains around PD allow for reversible transient modifications in $\bar{\alpha}$ (***Abou-Saleh et al., 2018***). Additionally, molecules could pass in the wake of larger proteins/complexes/structures that modify PDs (e.g., tubule-forming

viruses (***Amari et al., 2010***)). Assessing the extent and time scales of temporal variations in PD boundaries and their implications remains an open topic for future investigation.

The framework we have developed for so-called "simple" PDs also provides an intuition for the functional implications of complex geometries such as "twinned", "branched" or "funnel" PDs (***Ehlers and Kollmann, 2001***; ***Ehlers and van Bel, 2010***; ***Faulkner et al., 2008***; ***Ross-Elliott et al., 2017***). All else remaining equal, "twinned" PDs have twice the entrance surface area, which would result in doubling the effective permeability $P(\alpha)$. This increase, however, will be reduced because of the less uniform PD spacing in a density dependent manner (***Figure 7***A). "Branched" or "complex" PDs contain multiple sub-channels (branches) on at least one side with typically a single shared central cavity connecting all branches (***Oparka et al., 1999***; ***Roberts et al., 2001***; ***Fitzgibbon et al., 2013***). In the leaf sink/source transition, massive branching is observed and, coincidentally, the number of PDs is reduced (***Roberts et al., 2001***). The formation of many channels per PD could help to maintain sufficient transport capacity for smaller molecules. If so, the increase in the number of typically narrower channels should be much larger than the decrease in total (simple or complex) PD number. Our computations of f_{ih} after twinning suggest that minimizing the distance between sub-channels could be favourable at low to moderate PD densities (***Figure 7***C). "Funnel" PDs are reported in tissues surrounding the phloem (***Ross-Elliott et al., 2017***) and show a wide opening on the PSE (protophloem sieve element) side and a narrow opening on the PPP (phloem pole pericycle) side. (***Ross-Elliott et al., 2017***) model these as a triangular funnel that reaches its narrowest diameter only at the (PPP) bottom. There appears to be, however, a longer neck-like region at the narrow end of variable length. As hindrance is by far the highest in the narrowest section, the length of this narrow part would be a vital parameter in correctly estimating the transport permeabilities of these PDs.

Applying our model for diffusion as a sole driver of symplastic transport can indeed explain experimentally observed measurements of effective symplastic permeability for CF, but only with somewhat wider PDs/neck regions or several fold higher PD densities than usually measured by EM. Of these, the increased radius is the more plausible scenario, in line with the requirements for efficient GFP transport reported to occur among root meristem cells (***Benitez-Alfonso et al., 2009***, ***2013***; ***Nicolas et al., 2017b***), and similar to R_c values reporter in thicker cell walls (***Zhu et al., 1998***; ***Grison et al., 2015***; ***Nicolas et al., 2017b***). Our model can also explain the effect on permeability after treatment with high and low concentrations of H_2O_2 in ***Rutschow et al.*** (***2011***). The reduced permeability after high H_2O_2 treatment could be explained by a redox induced stress response and corresponding reduction of PD aperture (e.g., at a density of 10 PD/μm^2, a reduction from $\bar{\alpha}$ = 4.2 - 5.2 nm to $\bar{\alpha}$ = 1.5 nm would be required, see ***Table 1***B), whereas the strongly increased permeability could most plausibly be explained by a ±4 fold increase in PD density through two rounds of PD twinning / duplication. Studies on the formation of complex PDs (which often show many entrances) during the sink-source transition in leaves indicate that such could be possible within the applied incubation period of 2 hours (***Roberts et al., 2001***; ***Fitzgibbon et al., 2013***). The fact is that to reproduce experimentally measured CF effective permeabilities with our model, we had to deviate from ultrastructural based values for at least one parameter. Potential sources for these variations are: 1) ultrastructural studies might underestimate R_n because plants respond to pre-EM manipulation by closing PDs, 2) PDs could be destroyed during processing for TEM leading to an underestimation of PD densities, 3) the mechanical properties of cell walls and membranes provide a flexibility in the channel that could to some degree accommodate molecules larger than the apparent R_n. For a passive transport mechanism, the elastic energy required for these reversible deformations would have to be in the order of a few k_BT or less. Despite these deviations, comparing our model to the sub-nano channel model, we found that the latter requires roughly twice as high PD densities to produce the same permeability values $P(CF)$. Besides the observation of axial spokes rather than longitudinal channels on longitudinal sections (***Ding et al., 1992***; ***Nicolas et al., 2017b***), it is difficult to envision how the sub-nano channel model would allow for dynamic regulation of size selectivity through callose accumulation in the surrounding cell wall. These

considerations render the unobstructed sleeve model more attractive. In the future, this model could be refined with the consideration of central spokes ***Ding et al.*** (***1992***); ***Nicolas et al.*** (***2017b***) and variability of PD dimensions within a single cell wall ***Nicolas et al.*** (***2017b***); ***Yan et al.*** (***2019***).

Technological advances have started to be applied for more refined determinations on ultrastructural parameters. New fixation and sectioning techniques and new technologies such as cryoEM and Correlative Fluorescence Electron Microscopy (CFEM) are now part of the systematic study of PD connections in different plant cells, tissues and organs. In parallel, new information on structural features characterizing PD in different plant species/developmental stages as well as on the factors controlling PD structure and function (and thereby the effective permeability of specific molecules in different developmental or environmental conditions) are emerging. Combined with this significant experimental progress, our calculations provide a functional interpretation to characteristic PD morphological features and provide a framework to investigate how transport properties depend on these ultrastructural features and particle size in the context of simple and complex PD geometries. Another level of predictive power could be unlocked by integrating our framework into larger models at the tissue to whole organism level. This opens new avenues for exploring how developmental regulation of symplastic transport interacts with various other pathways for long and short range intercellular communication.

Methods

Diffusive flux through a single PD

Similar to ***Smith*** (***1986***), we assumed the flux is distributed homogeneously within each cross section along the axis of the channel. This results in a simple mapping to a 1D channel, i.e. that the average local flux (per unit area of cross section) $\sim$ 1/available cross section surface. This assumption does not hold close to the transition between neck and central region, i.e., a sharp transition between narrow and wide cylinders. Numerical simulations showed, however, that the error introduced by the assumption of homogeneous flux turned out to less than 4 percent for $l = 200nm$, the shortest l with experimentally observed neck region in ***Nicolas et al.*** (***2017b***) (***Appendix 2 Figure 1***) and will be less for longer channels. This error can be considered irrelevant given the quality of available data on PD dimensions and the many molecular aspects of PD functioning that are necessarily neglected in a simple model.

Hindrance factors

Hindrance factors $H(\lambda)$ including both steric and hydrodynamic effects are modelled using the numerical approximations in ***Dechadilok and Deen*** (***2006***). They present functions for cylindrical and slit pores. For PDs with a desmotubule, we use the function calculated for straight slits.

$$H(\lambda) = 1 + \frac{9}{16}\lambda\ln(\lambda) - 1.19358\lambda + 0.4285\lambda^3 - 0.3192\lambda^4 + 0.08428\lambda^5. \quad (8)$$

This choice is supported by the steric hindrance prefactor that is included in $H(\lambda)$ ***Dechadilok and Deen*** (***2006***). This $\Phi(\lambda) = 1 - \lambda$ is the same as the ratio of available to full surface area $\tilde{A}_x(\alpha)/A_x$. For cylindrical channels, i.e., reference channels in ***Figure 5*** and the regular PDs after DT removal, we use

$$\begin{aligned} H_c(\lambda) = {} & 1 + \frac{9}{8}\lambda\log(\lambda) - 1.56034\lambda + 0.528155\lambda^2 + 1.91521\lambda^3 - 2.81903\lambda^4 \\ & + 0.270788\lambda^5 + 1.10115\lambda^6 - 0.435933\lambda^7 \end{aligned} \quad (9)$$

for $\lambda < 0.95$ and the asymptotic approximation by ***Mavrovouniotis and Brenner*** (***1988***),

$$H_c(\lambda) = (1-\lambda)^2 \cdot (0.984\left(\frac{1-\lambda}{\lambda}\right)^{\frac{5}{2}} \quad (10)$$

otherwise, as suggested by ***Dechadilok and Deen*** (***2006***).

Relative molar flow rate and MRT

For assessing the impact of the neck constriction on PD transport, we defined two relative quantities: $Q_{rel} = Q_{necked}/Q_{narrow}$ and $\tau_{rel} = \tau_{necked}/\tau_{narrow}$ (***Figure 4***, ***Appendix 3 Figure 1***). Using ***Equation 2*** for $Q(\alpha)$, Q_{rel} is well defined:

$$Q_{rel}(\alpha, R_c) = \frac{l\tilde{\tilde{A}}_c}{2(\tilde{l}_n)\tilde{\tilde{A}}_c + (l - 2\tilde{l}_n)\tilde{\tilde{A}}_n} \tag{11}$$

$$\lim_{R_c \to \infty} Q_{rel}(\alpha, R_c) = \frac{l}{2\tilde{l}_n} \tag{12}$$

For τ_{rel} we first needed an expression for τ itself. Ideally, this would be a MFPT, which could calculated in a way similar to $\tau_{\|}$ in the calculation of f_{ih}, using a narrow-wide-narrow setup. These calculations, however, critically depend on trapping rates at the narrow-wide transitions. We do not have an expression for these, because the DT takes up the central space of the channel, which, contrary to the case of f_{ih}, substantially alters the problem and the circular trap based calculations would result in an underestimation of the MFPT. Instead, we stuck to the homogeneous flux assumption also used for $Q(\alpha)$ and defined τ as the corresponding estimate for the mean residence time (MRT) in the channel (see ***Equation 5***). Elaborating ***Equation 5***:

$$\tau(\alpha) = \frac{C_l + C_0}{2D\Delta C} \frac{(2\tilde{l}_n\tilde{\tilde{A}}_n + (l - 2\tilde{l}_n)\tilde{\tilde{A}}_c)(2\tilde{l}_n\tilde{\tilde{A}}_c + (l - 2\tilde{l}_n)\tilde{\tilde{A}}_n)}{\tilde{\tilde{A}}_n\tilde{\tilde{A}}_c} \tag{13}$$

$$= \frac{C_l + C_0}{2D\Delta C}\left(4\tilde{l}_n^2 + (l - 2\tilde{l}_n)^2 + 2\tilde{l}_n(l - 2\tilde{l}_n)\left(\frac{\tilde{\tilde{A}}_c}{\tilde{\tilde{A}}_n} + \frac{\tilde{\tilde{A}}_c}{\tilde{\tilde{A}}_n}\right)\right). \tag{14}$$

Unfortunately, this depends on the concentration difference over the channel. We are interested, however, in how the MRT changes with increasing R_c. In our definition of τ_{rel}, the concentration difference cancels from the equation, solving the problem:

$$\tau_{rel}(\alpha, R_c) = \frac{1}{l^2}\left(4\tilde{l}_n^2 + (l - 2\tilde{l}_n)^2 + 2\tilde{l}_n(l - 2\tilde{l}_n)\left(\frac{\tilde{\tilde{A}}_c}{\tilde{\tilde{A}}_n} + \frac{\tilde{\tilde{A}}_c}{\tilde{\tilde{A}}_n}\right)\right). \tag{15}$$

This method of computing τ_{rel} again depends on the homogeneous flux assumption. For an estimate of the error introduced by this approach, see ***Appendix 2***.

Flow towards PDs: correction for inhomogeneity of the wall permeability

To compute f_{ih}, we consider a linear chain of cells that are symplastically connected over their transverse walls (***Figure 1***). We first compute mean first passage time (MFPT) $\tau_{\|}$ through a simplified PD and a column of cytoplasm surrounding it. We then convert $\tau_{\|}$ to an effective wall permeability and compare the result with the uncorrected effected permeability computed using ***Equation 6*** for the simplified PD geometry and $f_{ih} = 1$.

As a simplified PD, we use a narrow cylindrical channel of length l and radius R_n, i.e., initially without DT. We assume that PDs are regularly spaced on a triangular grid. Consequently, the domain of cytoplasm belonging to each PD is a hexagonal column of length L, the length of the cell (***Figure 6***). We adjust the results reported by ***Makhnovskii et al.*** (***2010***) for cylindrical tubes with alternating diameter by changing the wide cylinder of radius R_w with a hexagonal column with cross section area $A_w = 1/\rho$ and considering hindrance effects. Makhnovskii *et al.* use a setup with an absorbing plane in the middle of a wide section and a reflecting plane, where also the initial source is located, in the middle of the next wide section. Assuming equal diffusion constants in both sections, they report the following MFPT from plane to plane:

$$\tau_{\|} = \frac{1}{2D}\left[L^2 + l^2 + 2D\left(\frac{l}{\kappa_n} + \frac{L}{\kappa_w}\right) + lL\left(\frac{\kappa_w}{\kappa_n} + \frac{\kappa_n}{\kappa_w}\right)\right], \tag{16}$$

where

$$\kappa_w = \frac{4DR_n f(\frac{R_n^2}{R_w^2})}{\pi R_w^2} \tag{17}$$

is a trapping rate to map the 3D setup onto a 1D diffusion problem. In this,

$$f(\sigma) = \frac{1 + A\sqrt{\sigma} - B\sigma^2}{(1-\sigma)^2} \tag{18}$$

is a function that monotonically increases from 0 to infinity as σ, the fraction of the wall occupied by the circular PDs, increases from 0 to 1. $f(\sigma)$ is the result of a computer assisted boundary homogenization procedure with the values of A and B depending on the arrangement of trapping patches (***Berezhkovskii et al., 2006***). To maintain detailed balance, the corresponding trapping rate κ_n must satisfy $A_w\kappa_w = A_n\kappa_n$, with A_x the respective cross section areas of both tubes.

As PDs are very narrow, we must take into account that only part of the cross section surface inside the PD is available to a particle of size α. Additionally, a subtle problem lies in the determination of R_w, as it is impossible to create a space filling packing with cylinders. To solve both issues, we rewrite ***Equation 16*** to explicitly contain cross section surfaces. We then replace A_n with $\tilde{\tilde{A}}_n$ to accommodate hindrance effects and we replace A_w by $1/\rho$. We also ajust PD length: $\tilde{l} = l + 2\alpha$ and $L = L - 2\alpha$. At the same time, we adjust $f(\sigma)$ to match a triangular distribution of the simplified PDs by using $A = 1.62$ and $B = 1.36$ (***Berezhkovskii et al., 2006***), which produces the hexagonal cytoplasmic column shape. This yields:

$$\tau_\parallel = \frac{1}{2D}\left[\tilde{L}^2 + \tilde{l}^2 + 2D\left(\frac{\tilde{l}}{\kappa_n} + \frac{\tilde{L}}{\kappa_w}\right) + \tilde{l}\tilde{L}\left(\tilde{\tilde{A}}_n\rho + \frac{1}{\tilde{\tilde{A}}_n\rho}\right)\right]. \tag{19}$$

We similarly adjust κ_w:

$$\kappa_w = 4\rho D H_c(\alpha/R_n) R_n f(\rho\tilde{A}_n), \tag{20}$$

where $H_c(\lambda)$ is the hindrance factor for cylindrical pores (see methods). In the same fashion, we also adjust κ_n.

We then invert the relation $\tau_\parallel = \frac{L^2}{2D} + \frac{L}{2P_{eff}}$, where we write P_{eff} for the effective wall permeability (***Makhnovskii et al., 2009***), to obtain $P_{eff} = \frac{L}{2\tau_\parallel - L^2/D}$. With this, we can compute $f_{ih} = P_{eff}/(\rho\Pi(\alpha))$, where $\Pi(\alpha)$ is calculated using the same PD geometry. To validate the choice of boundary placement underlying the calculations above, we also calculated the MFPT over two PD passages, i.e., by shifting the reflecting boundary to the middle of one cell further. This resulted in a 4-fold increase of $\tau_\parallel$ and L^2 and hence in exactly the same P_{eff}.

To assess whether the desmotubule has a large impact on f_{ih}, we further adapt ***Equation 19*** by replacing $\tilde{\tilde{A}}_n$ by our desmotubule corrected $\tilde{\tilde{A}}_n$, except in $f(\sigma)$. Additionally, we multiply $f(\sigma)$ by $\xi = (\tilde{R}_n^2 - \tilde{R}_{dt}^2)/\tilde{R}_n^2$. Numerical calculations in a simple trapping setup confirm the validity of reducing $f(\sigma)$ proportional to the area occupied by the desmotubule whilst calculating σ based on the outer radius alone (***Appendix 4 Figure 1*** and ***Appendix 4***). This is in agreement with results for diffusion towards clusters of traps in 3D (***Makhnovskii et al., 2000***). By the same reasoning, we introduced a hindrance factor in κ_w. Finally, we adjust the hindrance factors to a slit geometry as before. This results in:

$$\tau_\parallel = \frac{1}{2D}\left[\tilde{L}^2 + \tilde{l}^2 + \frac{\tilde{L}/\rho + \tilde{l}\tilde{\tilde{A}}_n}{2R_n H(2\alpha/(R_n - R_{dt}))\xi f(\rho\tilde{A}_n)} + \tilde{l}\tilde{L}\left(\tilde{\tilde{A}}_n\rho + \frac{1}{\tilde{\tilde{A}}_n\rho}\right)\right]. \tag{21}$$

To investigate the effect of different PD distributions, we used all relevant pairs of A and B in $f(\sigma)$ for different regular trap distributions as given in ***Berezhkovskii et al.*** (***2006***). As A_w is calculated implicitly from $1/\rho$, no other adjustments were necessary.

Correction factor f_{ih} for pit fields

For computing f_{ih} in pit fields, we used a two step approach similar to computing f_{ih} including DT as described above. A similar approach is also followed for the sub-nano channel model. In this calculation, a single pit field is modelled as a number of PDs on a triangular (or square) grid with a centre-to-centre distance d between nearest neighbours. We then calculate the pit radius, R_{pit} as the radius of the circle that fits the outer edges of the PD entrances. In the trivial case of one PD per

"pit", $R_{pit} = R_n$. For larger numbers of PDs per pit, see ***Table 2***. For this calculation, individual PDs are modelled as straight cylindrical PDs with radius R_n. We calculate a $\tau_{\parallel}$ based on circular traps with radius R_{pit} and a reduced efficiency based on the fraction of the pit that is occupied by the circular PDs. We accordingly adjust $\kappa_{w,pit}$ and $\tau_{\parallel,pit}$:

$$\kappa_{w,pit} = 4\rho D H_c(\alpha/R_{pit}) R_{pit} \xi f(\rho\pi\tilde{R}_{pit}^2), \tag{22}$$

where p is the number of PDs per pit and $\xi = p\tilde{R}_n^2/\tilde{R}_{pit}^2$ is the fraction of available pit area that is occupied by available PD area, and

$$\tau_{\parallel} = \frac{1}{2D}\left[\tilde{L}^2 + \tilde{l}^2 + \frac{\tilde{L}/\rho + \tilde{l}p\tilde{\tilde{A}}_n}{2R_{pit}H(\alpha/R_{pit})\xi f(\rho\tilde{A}_{pit})} + \tilde{l}\tilde{L}\left(p\tilde{\tilde{A}}_n\rho + \frac{1}{p\tilde{\tilde{A}}_n\rho}\right)\right]. \tag{23}$$

In these equations, ρ is the total PD density. In our graphs, we either keep ρ constant while increasing p to investigate the effect of clustering, resulting in a pit density ρ_{pits} of ρ/p, or keep ρ_{pits} constant to investigate the effect of (repeated) PD twinning. As a default, we used $d = 120$ nm based on distances measured from pictures in (***Faulkner et al., 2008***) of basal cell walls of *Nicotinia tabacum* leaf trichomes. To verify our calculations, we compared them with a single step calculation with large circles only, i.e., with radius R_{pit} and density ρ/p. As results in 3D suggest that for strongly absorbing clusters, the outer radius and cluster density dominate the diffusion (survival time) process (***Makhnovskii et al., 2000***), this should produce a lower bound to f_{ih}. In terms of PDs, this regime applies if a particle that reaches a pit field also has a high probability of entering in it. Indeed, the values calculated with the two step method above were similar and somewhat larger than with the simple large patch method, showing that our computation method is reasonable.

Only a relatively small fraction of the pits is occupied by the PD entrances (5-10% when modelled as circles with $R_n = 14$ nm and 3-7% with $R_n = 12$ nm.). Consequently, this approach may become inaccurate when R_{pit} gets too large. We indeed found instances where $f_{ih,pits}$ was larger than $f_{ih,singlePDs}$. In those cases, R_{pit} was in the order of $d_{pit}/4$ or larger. We assume that in those cases, the clusters are so close, that the clustering has only minor impact on f_{ih}, and f_{ih} is better estimated by the calculation for single PDs.

Computing required densities or $\bar{\alpha}$ with default model

Numbers in ***Table 1*** are computed based on forward computation of $P(\alpha)$ given ρ, $\bar{\alpha}$, corresponding R_n and other parameters with increments of 0.1 PD/μm^2 (ρ) or 0.01 nm ($\bar{\alpha}$ etc.) and linear interpolation between the two values that closest match the target $P(\alpha)$. This yields an error of less than 0.0001 $\mu m/s$ on $P(\alpha)$. We use $\alpha = 0.5$ nm for CF. The method for computing $P(CF)$ using the unobstructed sleeve (default) model is described throughout the main text. PDinsight, the python program used for computing all values in ***Table 1***, ***Appendix 5***, ***Figure 8***B and ***Table 2*** is available as supporting material.

Acknowledgements

The authors thank Dr. E.M. Bayer and Lysiane Brocard from the Bordeaux Imaging Centre, Plant Imaging Platform, University of Bordeaux, France, for providing the electron micrograph included in ***Figure 1***. Also we thank Philip Kirk (Centre for Plant Sciences, Leeds) for critical review of the python program.

Competing interests

The authors declare that there are no competing interests, financial or otherwise.

References

Abou-Saleh RH, Hernandez-Gomez MC, Amsbury S, Paniagua C, Bourdon M, Miyashima S, Helariutta Y, Fuller M, Budtova T, Connell SD, et al. Interactions between callose and cellulose revealed through the analysis of biopolymer mixtures. Nature communications. 2018; 9.

Table 2. Pit radius (R_{pit}) as a function of number of PDs per pit. The third and fourth column show numerical values for $d = 120$ nm and $R_n = 12$. *: All entries are based on PDs on a triangular grid within each pit, except for 4 and 5, where the PDs inside a pit are arranged on a square grid. Clusters (pitfields) are always arranged on a triangular grid.

PDs/pit	R_{pit}	A_{PD}/A_{pit}	R_{pit}
1	R_n	1	12
2	$R_n + \frac{1}{2}d$	0.056	72
3	$R_n + \frac{1}{3}\sqrt{3}d$	0.065	81.3
4*	$R_n + \frac{1}{2}\sqrt{2}d$	0.061	96.9
5*	$R_n + d$	0.041	132
6	$R_n + \frac{2}{3}\sqrt{3}d$	0.038	150.6
7	$R_n + d$	0.058	132
12	$R_n + \frac{1}{3}\sqrt{13}d$	0.071	156.2
19	$R_n + 2d$	0.043	252

Amari K, Boutant E, Hofmann C, Schmitt-Keichinger C, Fernandez-Calvino L, Didier P, Lerich A, Mutterer J, Thomas CL, Heinlein M, Mély Y, Maule AJ, Ritzenthaler C. A Family of Plasmodesmal Proteins with Receptor-Like Properties for Plant Viral Movement Proteins. PLOS Pathogens. 2010 09; 6(9):1–10. https://doi.org/10.1371/journal.ppat.1001119, doi: 10.1371/journal.ppat.1001119.

Amsbury S, Kirk P, Benitez-Alfonso Y. Emerging models on the regulation of intercellular transport by plasmodesmata-associated callose. Journal of experimental botany. 2017; 69(1):105–115.

Benitez-Alfonso Y, Cilia M, Roman AS, Thomas C, Maule A, Hearn S, Jackson D. Control of Arabidopsis meristem development by thioredoxin-dependent regulation of intercellular transport. Proc Natl Acad Sci U S A. 2009 Mar; 106(9):3615–3620. http://dx.doi.org/10.1073/pnas.0808717106, doi: 10.1073/pnas.0808717106.

Benitez-Alfonso Y, Faulkner C, Pendle A, Miyashima S, Helariutta Y, Maule A. Symplastic intercellular connectivity regulates lateral root patterning. Developmental cell. 2013; 26(2):136–147.

Benitez-Alfonso Y, Faulkner C, Ritzenthaler C, Maule AJ. Plasmodesmata: gateways to local and systemic virus infection. Mol Plant Microbe Interact. 2010 Nov; 23(11):1403–1412. http://dx.doi.org/10.1094/MPMI-05-10-0116, doi: 10.1094/MPMI-05-10-0116.

Berezhkovskii AM, Monine MI, Muratov CB, Shvartsman SY. Homogenization of boundary conditions for surfaces with regular arrays of traps. J Chem Phys. 2006 Jan; 124(3):036103. http://dx.doi.org/10.1063/1.2161196, doi: 10.1063/1.2161196.

Blake JR. On the hydrodynamics of plasmodesmata. J Theor Biol. 1978 Sep; 74(1):33–47.

Calvert P, Peet J, Bragin A, Schiesser W, Pugh Jr E. Fluorescence relaxation in 3D from diffraction-limited sources of PAGFP or sinks of EGFP created by multiphoton photoconversion. Journal of microscopy. 2007; 225(1):49–71.

Champion D, Hervet H, Blond G, Simatos D. Comparison between two methods to measure translational diffusion of a small molecule at subzero temperature. Journal of agricultural and food chemistry. 1995; 43(11):2887–2891.

Chudakov DM, Lukyanov S, Lukyanov KA. Tracking intracellular protein movements using photoswitchable fluorescent proteins PS-CFP2 and Dendra2. Nature protocols. 2007; 2(8):2024.

Comtet J, Turgeon R, Stroock A. Phloem loading through plasmodesmata: a biophysical analysis. Plant physiology. 2017; p. pp–01041.

Corti H, Frank G, Marconi M. An alternate solution of fluorescence recovery kinetics after spot-bleaching for measuring diffusion coefficients. 2. Diffusion of fluorescein in aqueous sucrose solutions. Journal of solution chemistry. 2008; 37(11):1593–1608.

Crawford KM, Zambryski PC. Subcellular localization determines the availability of non-targeted proteins to plasmodesmatal transport. Curr Biol. 2000 Sep; 10(17):1032–1040.

694 **Danila FR**, Quick WP, White RG, Furbank RT, von Caemmerer S. The Metabolite Pathway between Bundle Sheath
695 and Mesophyll: Quantification of Plasmodesmata in Leaves of C3 and C4 Monocots. The Plant Cell. 2016;
696 28(6):1461–1471. http://www.plantcell.org/content/28/6/1461, doi: 10.1105/tpc.16.00155.

697 **Dashevskaya S**, Kopito RB, Friedman R, Elbaum M, Epel BL. Diffusion of anionic and neutral GFP derivatives
698 through plasmodesmata in epidermal cells of Nicotiana benthamiana. Protoplasma. 2008 Dec; 234(1-4):13–23.
699 http://dx.doi.org/10.1007/s00709-008-0014-7, doi: 10.1007/s00709-008-0014-7.

700 **Dechadilok P**, Deen WM. Hindrance factors for diffusion and convection in pores. Industrial & Engineering
701 Chemistry Research. 2006; 45(21):6953–6959.

702 **Ding B**, Turgeon R, Parthasarathy M. Substructure of freeze-substituted plasmodesmata. Protoplasma. 1992;
703 169(1):28–41.

704 **Douglas J**, Gunn JE. A general formulation of alternating direction methods. Numerische Mathematik. 1964;
705 6(1):428–453.

706 **Ehlers K**, Kollmann R. Primary and secondary plasmodesmata: structure, origin, and functioning. Protoplasma.
707 2001; 216(1-2):1–30.

708 **Ehlers K**, van Bel AJE. Dynamics of plasmodesmal connectivity in successive interfaces of the cambial zone.
709 Planta. 2010 Jan; 231(2):371–385. http://dx.doi.org/10.1007/s00425-009-1046-8, doi: 10.1007/s00425-009-
710 1046-8.

711 **Faulkner C**, Akman OE, Bell K, Jeffree C, Oparka K. Peeking into pit fields: a multiple twinning model of secondary
712 plasmodesmata formation in tobacco. Plant Cell. 2008 Jun; 20(6):1504–1518. http://dx.doi.org/10.1105/tpc.
713 107.056903, doi: 10.1105/tpc.107.056903.

714 **Fitzgibbon J**, Beck M, Zhou J, Faulkner C, Robatzek S, Oparka K. A developmental framework for complex
715 plasmodesmata formation revealed by large-scale imaging of the Arabidopsis leaf epidermis. The Plant Cell.
716 2013; p. tpc–112.

717 **Gallagher KL**, Sozzani R, Lee CM. Intercellular protein movement: deciphering the language of development.
718 Annual review of cell and developmental biology. 2014; 30:207–233.

719 **Gerlitz N**, Gerum R, Sauer N, Stadler R. Photoinducible DRONPA-s: a new tool for investigating cell–cell
720 connectivity. The Plant Journal. 2018; 94(5):751–766.

721 **Goodwin PB**, Shepherd V, Erwee MG. Compartmentation of fluorescent tracers injected into the epidermal cells
722 of <i>Egeria densa</i> leaves. Planta. 1990; 181:129–136. http://dx.doi.org/10.1007/BF00202335,
723 10.1007/BF00202335.

724 **Grison MS**, Brocard L, Fouillen L, Nicolas W, Wewer V, Dörmann P, Nacir H, Benitez-Alfonso Y, Claverol S, Germain
725 V, et al. Specific membrane lipid composition is important for plasmodesmata function in Arabidopsis. The
726 Plant Cell. 2015; p. tpc–114.

727 **Gunning B**, Hughes J. Quantitative assessment of symplastic transport of pre-nectar into the trichomes of
728 Abutilon nectaries. Functional Plant Biology. 1976; 3(5):619–637.

729 **Haritatos E**, Keller F, Turgeon R. Raffinose oligosaccharide concentrations measured in individual cell and tissue
730 types in Cucumis melo L. leaves: implications for phloem loading. Planta. 1996; 198(4):614–622.

731 **Haywood V**, Kragler F, Lucas WJ. Plasmodesmata: pathways for protein and ribonucleoprotein signaling. Plant
732 Cell. 2002; 14 Suppl:S303–S325.

733 **Jensen KH**, Mullendore DL, Holbrook NM, Bohr T, Knoblauch M, Bruus H. Modeling the hydrodynamics
734 of Phloem sieve plates. Front Plant Sci. 2012; 3:151. http://dx.doi.org/10.3389/fpls.2012.00151, doi:
735 10.3389/fpls.2012.00151.

736 **Kankanala P**, Czymmek K, Valent B. Roles for rice membrane dynamics and plasmodesmata during biotrophic
737 invasion by the blast fungus. Plant Cell. 2007 Feb; 19(2):706–724. http://dx.doi.org/10.1105/tpc.106.046300,
738 doi: 10.1105/tpc.106.046300.

739 **Kim I**, Cho E, Crawford K, Hempel FD, Zambryski PC. Cell-to-cell movement of GFP during embryogenesis
740 and early seedling development in Arabidopsis. Proc Natl Acad Sci U S A. 2005 Feb; 102(6):2227–2231.
741 http://dx.doi.org/10.1073/pnas.0409193102, doi: 10.1073/pnas.0409193102.

Kim I, Hempel FD, Sha K, Pfluger J, Zambryski PC. Identification of a developmental transition in plasmodesmatal function during embryogenesis in Arabidopsis thaliana. Development. 2002 Mar; 129(5):1261–1272.

Knox K, Wang P, Kriechbaumer V, Tilsner J, Frigerio L, Sparkes I, Hawes C, Karl JO. Putting the squeeze on PDs-a role for RETICULONS in primary plasmodesmata formation. Plant physiology. 2015; p. pp–00668.

Liesche J, Schulz A. Quantification of plant cell coupling with three-dimensional photoactivation microscopy. J Microsc. 2012 Jul; 247(1):2–9. http://dx.doi.org/10.1111/j.1365-2818.2011.03584.x, doi: 10.1111/j.1365-2818.2011.03584.x.

Liesche J, Gao C, Binczycki P, Andersen SR, Rademaker H, Schulz A, Martens HJ. Direct Comparison of Leaf Plasmodesma Structure and Function in Relation to Phloem-Loading Type. Plant Physiology. 2019; 179(4):1768–1778. http://www.plantphysiol.org/content/179/4/1768, doi: 10.1104/pp.18.01353.

Liesche J, Patrick J. An update on phloem transport: a simple bulk flow under complex regulation. F1000Research. 2017; 6.

Liesche J, Schulz A. Modeling the parameters for plasmodesmal sugar filtering in active symplasmic phloem loaders. Front Plant Sci. 2013; 4:207. http://dx.doi.org/10.3389/fpls.2013.00207, doi: 10.3389/fpls.2013.00207.

Lu KJ, De Rybel B, van Mourik H, Weijers D. Regulation of intercellular TARGET OF MONOPTEROS 7 protein transport in the Arabidopsis root. Development. 2018; 145(2). http://dev.biologists.org/content/145/2/dev152892, doi: 10.1242/dev.152892.

Makhnovskii YA, Berezhkovskii A, Yang DY, Sheu SY, Lin S. Trapping by clusters of traps. Physical Review E. 2000; 61(6):6302.

Makhnovskii YA, Berezhkovskii A, Zitserman VY. Diffusion in a tube of alternating diameter. Chemical physics. 2010; 370(1-3):238–243.

Makhnovskii YA, Zitserman VY, Berezhkovskii A. Diffusion in quasi-one-dimensional structures with a periodic sharp narrowing of the cross section. Russian Journal of Physical Chemistry B. 2009; 3(2):313–319.

Maule AJ. Plasmodesmata: structure, function and biogenesis. Curr Opin Plant Biol. 2008 Dec; 11(6):680–686. http://dx.doi.org/10.1016/j.pbi.2008.08.002, doi: 10.1016/j.pbi.2008.08.002.

Maule AJ, Benitez-Alfonso Y, Faulkner C. Plasmodesmata - membrane tunnels with attitude. Curr Opin Plant Biol. 2011 Dec; 14(6):683–690. http://dx.doi.org/10.1016/j.pbi.2011.07.007, doi: 10.1016/j.pbi.2011.07.007.

Mavrovouniotis GM, Brenner H. Hindered sedimentation, diffusion, and dispersion coefficients for brownian spheres in circular cylindrical pores. Journal of Colloid and Interface Science. 1988; 124(1):269–283.

Miyashima S, Roszak P, Sevilem I, Toyokura K, Blob B, Heo Jo, Mellor N, Help-Rinta-Rahko H, Otero S, Smet W, et al. Mobile PEAR transcription factors integrate positional cues to prime cambial growth. Nature. 2019; 565(7740):490.

Nakajima K, Sena G, Nawy T, Benfey PN. Intercellular movement of the putative transcription factor SHR in root patterning. Nature. 2001 Sep; 413(6853):307–311. http://dx.doi.org/10.1038/35095061, doi: 10.1038/35095061.

Nicolas WJ, Grison MS, Bayer EM. Shaping intercellular channels of plasmodesmata: the structure-to-function missing link. Journal of Experimental Botany. 2017; 69(1):91–103.

Nicolas WJ, Grison MS, Trépout S, Gaston A, Fouché M, Cordelières FP, Oparka K, Tilsner J, Brocard L, Bayer EM. Architecture and permeability of post-cytokinesis plasmodesmata lacking cytoplasmic sleeves. Nature plants. 2017; 3(7):17082.

Olesen P. The neck constriction in plasmodesmata. Planta. 1979; 144(4):349–358.

Oparka KJ, Roberts AG, Boevink P, Cruz SS, Roberts I, Pradel KS, Imlau A, Kotlizky G, Sauer N, Epel B. Simple, but not branched, plasmodesmata allow the nonspecific trafficking of proteins in developing tobacco leaves. Cell. 1999 Jun; 97(6):743–754.

Otero S, Helariutta Y, Benitez-Alfonso Y. Symplastic communication in organ formation and tissue patterning. Current opinion in plant biology. 2016; 29:21–28.

788 **Roberts IM**, Boevink P, Roberts AG, Sauer N, Reichel C, Oparka KJ. Dynamic changes in the frequency and
789 architecture of plasmodesmata during the sink-source transition in tobacco leaves. Protoplasma. 2001;
790 218(1-2):31–44.

791 **Ross-Elliott TJ**, Jensen KH, Haaning KS, Wager BM, Knoblauch J, Howell AH, Mullendore DL, Monteith AG, Paultre
792 D, Yan D, et al. Phloem unloading in Arabidopsis roots is convective and regulated by the phloem-pole
793 pericycle. Elife. 2017; 6:e24125.

794 **Rutschow HL**, Baskin TI, Kramer EM. Regulation of solute flux through plasmodesmata in the root
795 meristem. Plant Physiol. 2011 Apr; 155(4):1817–1826. http://dx.doi.org/10.1104/pp.110.168187, doi:
796 10.1104/pp.110.168187.

797 **Sager RE**, Lee JY. Plasmodesmata at a glance. J Cell Sci. 2018; 131(11):jcs209346.

798 **Schmitz K**, Kühn R. Fine structure, distribution and frequency of plasmodesmata and pits in the cortex
799 ofLaminaria hyperborea andL. saccharina. Planta. 1982; 154(5):385–392.

800 **Schönknecht G**, Brown JE, Verchot-Lubicz J. Plasmodesmata transport of GFP alone or fused to potato virus X
801 TGBp1 is diffusion driven. Protoplasma. 2008; 232(3-4):143–152.

802 **Skopelitis DS**, Hill K, Klesen S, Marco CF, von Born P, Chitwood DH, Timmermans MC. Gating of miRNA
803 movement at defined cell-cell interfaces governs their impact as positional signals. Nature communications.
804 2018; 9(1):3107.

805 **Smith DM**. Restricted diffusion through pores with periodic constrictions. AIChE journal. 1986; 32(6):1039–1042.

806 **Spiegelman Z**, Lee CM, Gallagher KL. KinG Is a Plant-Specific Kinesin That Regulates Both Intra- and Intercellular
807 Movement of SHORT-ROOT. Plant Physiology. 2018; 176(1):392–405. http://www.plantphysiol.org/content/
808 176/1/392, doi: 10.1104/pp.17.01518.

809 **Stadler R**, Lauterbach C, Sauer N. Cell-to-cell movement of green fluorescent protein reveals post-phloem
810 transport in the outer integument and identifies symplastic domains in Arabidopsis seeds and embryos. Plant
811 Physiol. 2005 Oct; 139(2):701–712. http://dx.doi.org/10.1104/pp.105.065607, doi: 10.1104/pp.105.065607.

812 **Stadler R**, Wright KM, Lauterbach C, Amon G, Gahrtz M, Feuerstein A, Oparka KJ, Sauer N. Expression of
813 GFP-fusions in Arabidopsis companion cells reveals non-specific protein trafficking into sieve elements and
814 identifies a novel post-phloem domain in roots. Plant J. 2005 Jan; 41(2):319–331. http://dx.doi.org/10.1111/j.
815 1365-313X.2004.02298.x, doi: 10.1111/j.1365-313X.2004.02298.x.

816 **Terauchi M**, Nagasato C, Kajimura N, Mineyuki Y, Okuda K, Katsaros C, Motomura T. Ultrastructural study of
817 plasmodesmata in the brown alga Dictyota dichotoma (Dictyotales, Phaeophyceae). Planta. 2012; 236(4):1013–
818 1026.

819 **Terauchi M**, Nagasato C, Motomura T. Plasmodesmata of brown algae. Journal of Plant Research. 2015 Jan;
820 128(1):7–15. https://doi.org/10.1007/s10265-014-0677-4, doi: 10.1007/s10265-014-0677-4.

821 **Terry B**, Matthews E, Haseloff J. Molecular characterization of recombinant green fluorescent protein by
822 fluorescence correlation microscopy. Biochemical and biophysical research communications. 1995; 217(1):21–
823 27.

824 **Terry B**, Robards A. Hydrodynamic radius alone governs the mobility of molecules through plasmodesmata.
825 Planta. 1987 Jun; 171(2):145–157. doi: {10.1007/BF00391090}.

826 **Tilsner J**, Amari K, Torrance L. Plasmodesmata viewed as specialised membrane adhesion sites. Protoplasma.
827 2011 Jan; 248(1):39–60. http://dx.doi.org/10.1007/s00709-010-0217-6, doi: 10.1007/s00709-010-0217-6.

828 **Waigmann E**, Zambryski P. Tobacco mosaic virus movement protein-mediated protein transport between
829 trichome cells. The Plant Cell. 1995; 7(12):2069–2079.

830 **Wu S**, Gallagher KL. Intact microtubules are required for the intercellular movement of the SHORT-ROOT
831 transcription factor. The Plant Journal. 2013; 74(1):148–159.

832 **Wu S**, Gallagher KL. The movement of the non-cell-autonomous transcription factor, SHORT-ROOT relies on the
833 endomembrane system. The Plant Journal. 2014; 80(3):396–409. https://onlinelibrary.wiley.com/doi/abs/10.
834 1111/tpj.12640, doi: 10.1111/tpj.12640.

Xu M, Cho E, Burch-Smith TM, Zambryski PC. Plasmodesmata formation and cell-to-cell transport are reduced in decreased size exclusion limit 1 during embryogenesis in Arabidopsis. Proc Natl Acad Sci U S A. 2012 Mar; 109(13):5098–5103. http://dx.doi.org/10.1073/pnas.1202919109, doi: 10.1073/pnas.1202919109.

Yan D, Yadav SR, Paterlini A, Nicolas WJ, Petit JD, Brocard L, Belevich I, Grison MS, Vaten A, Karami L, et al. Sphingolipid biosynthesis modulates plasmodesmal ultrastructure and phloem unloading. . 2019; https://www.repository.cam.ac.uk/handle/1810/292558, doi: https://doi.org/10.17863/CAM.39719.

Zambryski P, Crawford K. Plasmodesmata: gatekeepers for cell-to-cell transport of developmental signals in plants. Annu Rev Cell Dev Biol. 2000; 16:393–421. http://dx.doi.org/10.1146/annurev.cellbio.16.1.393, doi: 10.1146/annurev.cellbio.16.1.393.

Zavaliev R, Ueki S, Epel BL, Citovsky V. Biology of callose (β-1,3-glucan) turnover at plasmodesmata. Protoplasma. 2011 Jan; 248(1):117–130. http://dx.doi.org/10.1007/s00709-010-0247-0, doi: 10.1007/s00709-010-0247-0.

Zhu T, Lucas W, Rost T. Directional cell-to-cell communication in theArabidopsis root apical meristem I. An ultrastructural and functional analysis. Protoplasma. 1998; 203(1):35–47.

Appendix 1

List of mathematical symbols

	Default	Description
α	0.5 nm for CF	Particle size
$\bar{\alpha}$		Maximum particle size that fits through a (model) PD
A_c		Cytoplasmic sleeve cross section area in the central region
$\tilde{A}_c$		Cytoplasmic sleeve cross section area in the central region adjusted for particle size (= steric hindrance only)
$\tilde{\tilde{A}}_c$		Cytoplasmic sleeve cross section area in the central region after cross sectional averaging (= full hindrance; $\tilde{\tilde{A}}_c = H(\lambda)A_c$)
A_n		Cytoplasmic sleeve cross section area in the neck region
C		Concentration
ΔC		Concentration difference (over the PD channel)
D	162 μm^2/s for CF	*Particle size dependent* diffusion constant
d_1	1 nm^3/s	Diffusion constant for particle of unit radius × 1 nm (dummy value to illustrate scaling behaviour)
f_{ih}		Correction factor for inhomogeneous wall permeability ($0 \leq f_{ih} \leq 1$)
$H(\lambda)$		Hindrance factor calculated for a slit pore geometry
$H_c(\lambda)$		Hindrance factor calculated for a cylindrical pore geometry
λ		Relative particle size at the respective location (for straight PDs: $\lambda = \alpha/\bar{\alpha}$)
l_n	25 nm	Neck length
$\tilde{l}_n$		Effective neck length for a given particle size ($\tilde{l}_n = l_n + \alpha$)
l	100, 200, 500 nm	Total PD length
L	10 μm	Cell length
R_c	17.5 nm	Central region radius
R_{dt}	8 nm	DT radius
$\tilde{R}_{dt}$		Particle size adjusted DT radius ($\tilde{R}_{dt} = R_{dt} + \alpha$)
R_n	12 nm	Neck radius
R_x		Central region or neck radius, depending on position
$\tilde{R}_x$		Particle size adjusted central region/neck radius ($\tilde{R}_x = R_x - \alpha$)
ρ		PD density
p	1	number of PDs per cluster (“pit field”)
$P(\alpha)$		symplastic permeability (for particles of size α) of the entire cell wall
$\Pi(\alpha)$		symplastic permeability (for particles of size α) of a single PD per unit of cell wall surface, without correction factor f_{ih} ($\Pi(\alpha) = \frac{P(\alpha)}{f_{ih}\rho}$).
$Q(\alpha)$		Molar flow rate through a single PD (for particles of size α)
Q_{rel}		Molar flow rate relative to a reference situation (straight PD)
$\tilde{Q}_{rel}$		Rescaled Q_{rel}: $\tilde{Q}_{rel} = (Q_{rel} - 1)/(\frac{l}{2\tilde{l}_n} - 1) + 1$
τ_{rel}		Mean residence time (MRT) inside PD relative to a reference situation (straight PD)
$\tilde{\tau}_{rel}$		Rescaled τ_{rel}: $\tilde{\tau}_{rel} = (\tau_{rel} - 1)l^2/(2\tilde{l}_n(l - 2\tilde{l}_n))$
$\tau_{\parallel}$		Mean first passage time (MFPT) through a cytoplasmic column of length L with a wall in the middle of it containing one central PD; Used for the calculation of f_{ih}

Appendix 2

Estimating systematic error due to homogeneous flux assumption

Molar flow rate

To estimate the error on the calculation of $Q(\alpha)$, we compared our analytical results (***Equation 2***) to numerical evaluations of the diffusion equations on a 2D cross section of the available surface of the model PD with neck, see ***Appendix 2 Figure 1***.

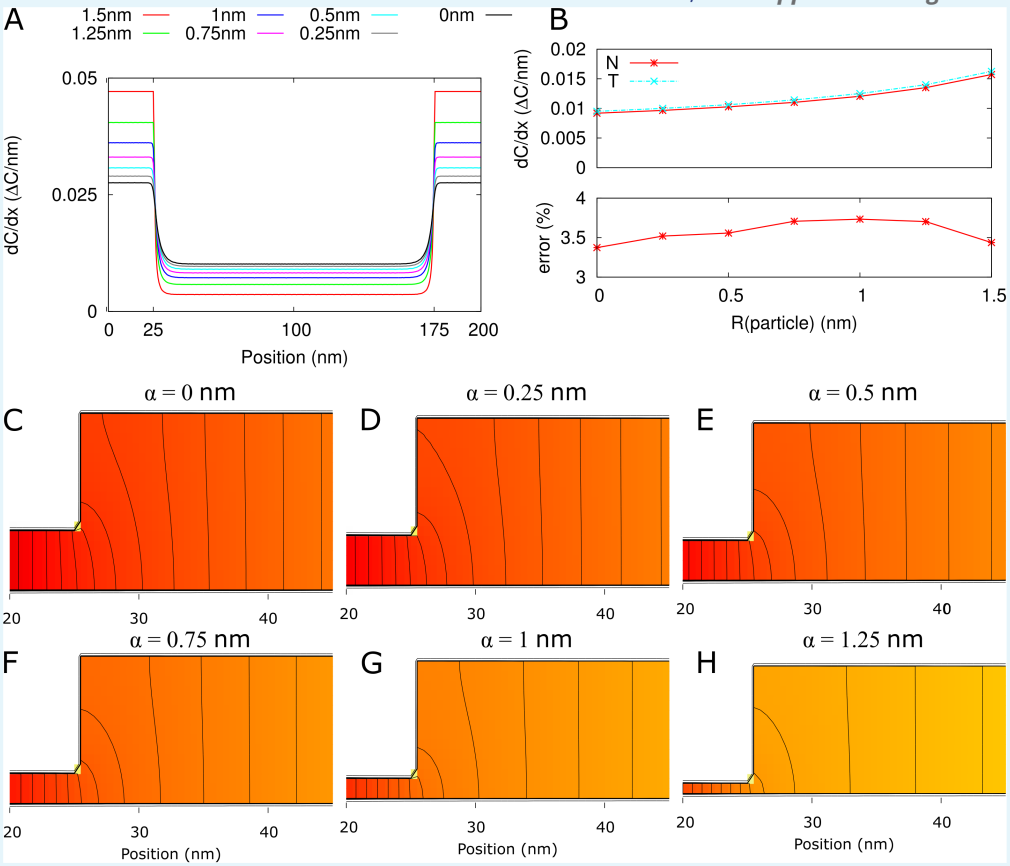

Appendix 2 Figure 1. Error of homogeneous flux approximation (all 2D). A: $\partial C/\partial x$ from numerical calculations (2D) along a straight line through the middle of the available neck region for different particle sizes. B: top: $\partial C/\partial x$ at neck entrance (proportional to the channel flux) from numerical calculations (N; solid red line with asterisks) and from 3-cylinder model with homogeneous flux assumption (T; dashed cyan line with crosses). The 3-cylinder model results in a consistent over estimation of $< 4\%$ (bottom). C-H: concentration heat maps for available part of the channel, focus on the neck/central region transition. The same color gradient is used for all six graphs. Black isolines are spaced at 1% of the total concentration difference over the channel. Parameters: $l = 200$ nm, defaults.

MRT

In absence of a DT, we can compute $\tau_{\parallel,PD}$ analogously to $\tau_{\parallel}$. This yields:

$$\tau_{\parallel,PD} = \frac{1}{2D}\left(4\tilde{l}_n^2 + (l-2\tilde{l}_n)^2 + 2\tilde{l}_n(l-2\tilde{l}_n)\left(\frac{\tilde{\tilde{A}}_c}{\tilde{\tilde{A}}_n} + \frac{\tilde{\tilde{A}}_c}{\tilde{\tilde{A}}_n}\right) + \frac{\tilde{V}_c + 2\tilde{V}_n}{2R_n H(\lambda_n) f(\tilde{A}_n/\tilde{A}_c)}\right), \quad (24)$$

with $\tilde{V}_x$ the hindrance adjusted volume of central region or single neck region. The expression in brackets is identical to the one in ***Equation 14***, except for the addition of the last term, meaning that τ is an underestimation of the MFPT. Using $\tau_{\parallel,PD}$ to define an alternative τ_{rel} for channels without DT, $\tau_{\parallel,rel}$, suggests that τ_{rel} is an underestimate of at least approximately 7-9% for $R_c = 17.5nm$ and $l = 100nm$ (***Appendix 2 Figure 2***). This factor saturates between 1.35 and 1.40 for all relevant particle sizes in the limit of unrealistically large R_c. For larger l, the factor has the same maximum values, but these are approached slower. Hence, the error is less for realistic R_c (e.g. 4-6% for $l = 200nm$ and 2-3% for $l = 500nm$.)

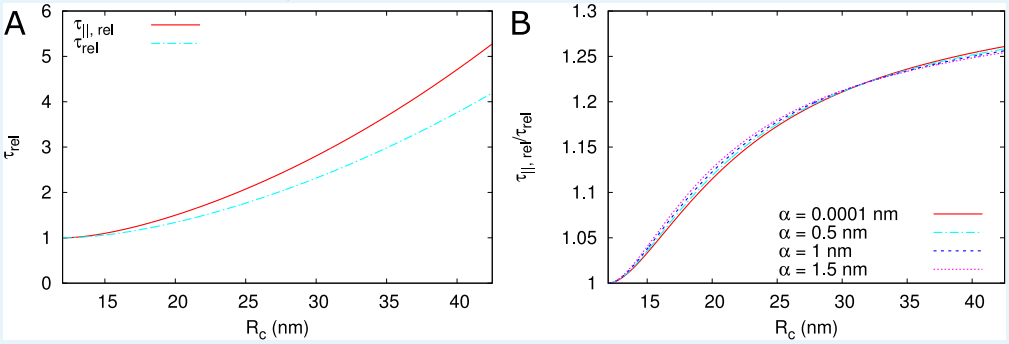

Appendix 2 Figure 2. Comparison of τ_{rel} as used in the main text against a $\tau_{\parallel,PD}$ based calculation ($\tau_{\parallel,rel}$). $l = 100nm,\ R_n = 12nm,\ R_{dt} = 8nm,\ l_n = 25nm.$

Appendix 3

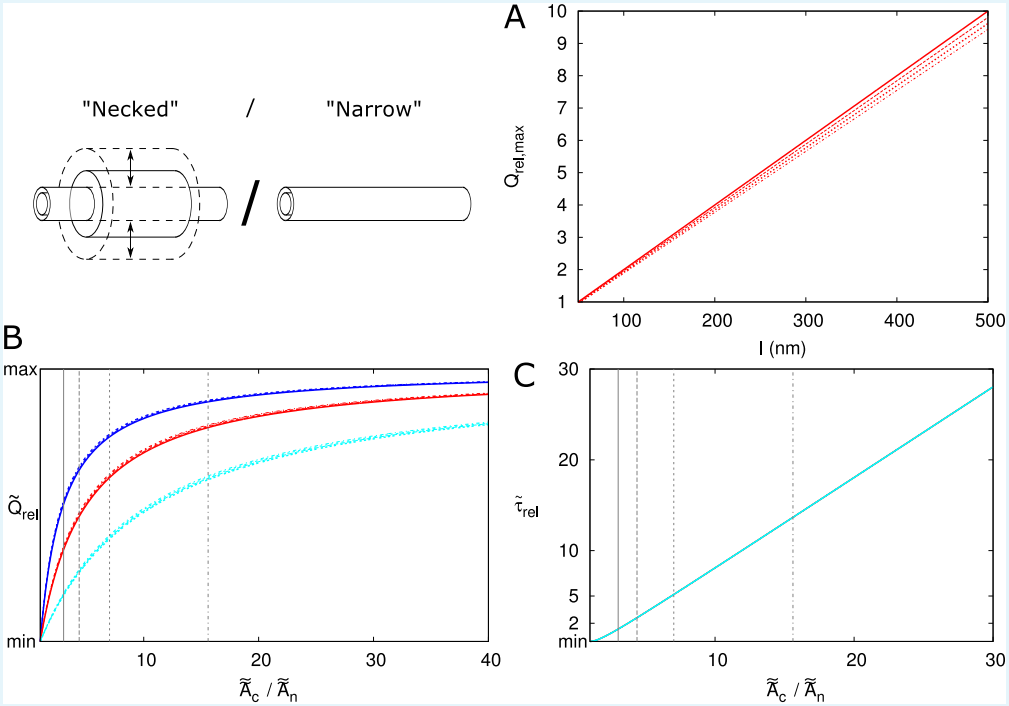

Appendix 3 Figure 1. Scaling of Q_{rel} and τ_{rel} through the PD. A: maximum possible increase of Q: $Q_{rel,max} = l/(2\tilde{l}_n)$. Line type indicates particle size (solid: $\alpha \approx 0$, dashed: $\alpha = 0.5nm$, sparse dashed: $\alpha = 1nm$, dash-dotted: $\alpha = 1.5nm$). B: curves for different α almost collapse with when plotted as function of $\tilde{A}_c/\tilde{A}_n$ and rescaled from the minimal value of 1 to $Q_{rel,max}$. The curves for different l do not collapse (blue: $l = 100nm$, red: $l = 200nm$, cyan: $l = 500nm$). C: curves for τ_{rel} collapse (for different l and α) with rescaling function $\tilde{\tau}_{re} = (\tau_{rel} - 1)l^2/(2\tilde{l}_n(l - 2\tilde{l}_n))$. Vertical lines in B,C correspond to $\tilde{\tilde{A}}_c/\tilde{\tilde{A}}_n$ for different particle sizes (line types as in A). Parameters: $l_n = 25nm$, $R_n = 12nm$, $R_{dl} = 8nm$.

Scaling behaviour of Q_{rel} and τ_{rel}

Rescaling of Q_{rel} and τ_{rel} is a way to collapse our understanding of the processes into simpler curves. The local flux is inversely proportional to the available cross section, motivating the ratio $\tilde{\tilde{A}}_c/\tilde{\tilde{A}}_n$ of the necked channel as a rescaling factor for the x-axis. Using the limit for Q_{rel} it is possible to almost completely collapse the curves for different particle sizes for a single l, l_n combination (***Appendix 3 Figure 1***B). For rescaling of τ_{rel}, we use its behaviour for large R_c:

$$\tau_{rel}(\alpha, R_c) \approx \frac{\tilde{\tilde{A}}_c(l - 2(\tilde{l}_n + \alpha))(2(\tilde{l}_n + \alpha))}{l^2\tilde{\tilde{A}}_n}, \qquad (R_c \to \infty) \tag{25}$$

$$\approx \frac{2\tilde{R}_c^2\tilde{l}_n(l - 2\tilde{l}_n)}{l^2(\tilde{R}_n^2 - \tilde{R}_{dl}^2)}, \qquad (R_c \to \infty). \tag{26}$$

For large R_c, τ_{rel} becomes proportional to $\tilde{R}_c^2$. From this we derived a rescaling factor for τ_{rel}: $\frac{1}{\tilde{f}_c(1-\tilde{f}_c)}$ with $\tilde{f}_c$ the fraction of PD length occupied by the central region (adapted for particle size), that collapses the curves for τ_{rel} for all α and l (***Appendix 3 Figure 1***C). The rescaling factor for the x-axis, $\tilde{\tilde{A}}_c/\tilde{\tilde{A}}_n$, increases faster for larger particles. The reason is that $\tilde{\tilde{A}}_n$ decreases relatively faster with particle size than $\tilde{\tilde{A}}_c$, which becomes intuitively clear from ***Figure 2***C,D. This difference explains why the curves for the largest particles are on top prior to rescaling (***Figure 4***). The τ_{rel}-rescaling factor implies that the MRT increases fastest if the central region occupies approximately half of the length of the channel. With our choice of a constant $l_n = 25nm$, this occurs at a wall thickness of $l \approx 100nm$.

Appendix 4

Numerical calculations for trapping rate of annular trap

Seen from the cytoplasmic bulk, the PD orifice has the shape of an annulus ("ring"). For our calculations above, however, we only have published trapping rates for circular traps. We tested two options for selecting an equivalent circular trap and trapping rate. For this, we numerically solved diffusion equations in a box with a single trap in the middle of one face and a source opposite to it (***Appendix 4 Figure 1***). In the x and y direction, we used periodic boundary conditions reflecting a periodic array of traps. In the z direction we fixed the concentration on side of the domain ("source plane") and used a radiating boundary condition with a mixed rate $\kappa(x,y) = k(x,y)D$ on the other side ("target plane"). We chose the trapping rate proportional to the diffusion constant, as the flux and molar flow rate through single PDs ($Q(\alpha)$) are proportional to D (***Equation 2***). For PDs, the target plane contained the "front view" of a single channel: an annulus with inner radius R_{di}, outer radius R_n and surface area A_{ann}. Within this annulus $k(x,y)$ was set to unity ($k(x,y)|_{PD} = 1/\mu m$) and 0 outside. For the corresponding homogeneous target plane $\kappa_{hom} = \frac{A_{ann}}{A_{total}}/\mu m$. At the grid level, the pixels at a boundary of the annulus had κ proportional to the fraction of their surface falling inside the annulus. The reference flux was computed analytically, exploiting that within each plane at a given distance z from the target plane, the concentration is the same everywhere. This allows for a trivial mapping to a 1D system. These 3D numerical calculations were performed using the Douglas method for 3D alternating direction implicit diffusion (***Douglas and Gunn, 1964***). To save computation time we used the analytically calculated reference profile as an initial condition for all calculations. We found that the annular patches gave the same result as circles with radius R_n and $k(x,y)|_{circ} = \frac{A_{ann}}{A_{circ}}/\mu m$, i.e. that the outer radius of the patch was most important (***Appendix 4 Figure 1***), In line with results for diffusion towards clusters of traps in 3D (***Makhnovskii et al., 2000***). These calculations support the choice of trapping rate in the calculation of f_{ih} including DT.

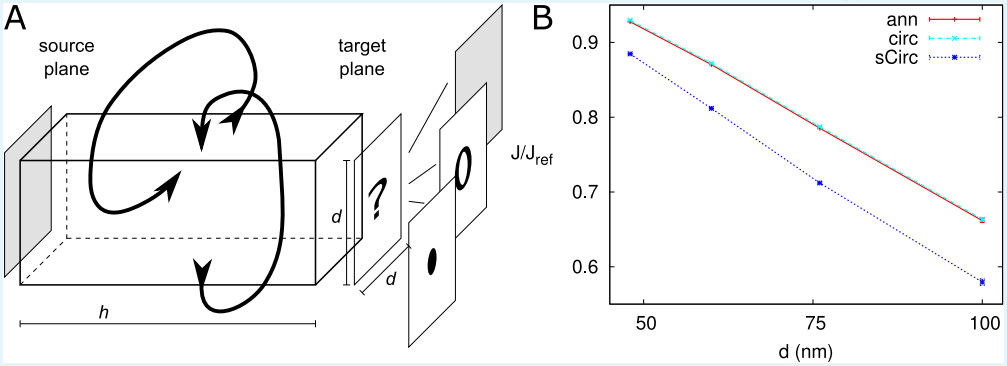

Appendix 4 Figure 1. Correction factor for annular trap shape. Comparison of discrete and homogeneous permeability. A: setup. A homogeneous source is located at a distance h from a trapping plane with either a single trap or homogeneous absorbency. The periodic boundary conditions in the other directions make that the traps are effectively spaced on a square grid with distance d between traps. B: Relative average net flux in direction of trap (component along the box) for PDs with DT ("ann": red) and circular channels with the same apparent surface ("sCirc": blue) and same outer radius, but trapping rate decreased according to surface ratios ("circ": cyan), $h = 300nm$. For both, the flux is compared with a homogeneous trap with rate $\kappa = \frac{A_{ann}}{A_{total}} D/\mu m$. Error bars (nearly invisible) represent the quality of the numerical estimate by minimum and maximum possible values.

Appendix 5

Computing required densities or $\bar{\alpha}$ with sub-nano model

Required densities or $\bar{\alpha}$ for the sub-nano model are computed with PDinsight similar to the default model. Additionally, we use the following approximations. For computing ρ_{sn} based on a given $\bar{\alpha}$, we compute a density multiplier based on n_c (***Equation 7***) and ***Figure 5***. This implicitly assumes that f_{ih} is not affected by the different PD density. For example, for $\bar{\alpha} = 2.5$ nm, a 16.8 (***Equation 7***) × 1.63 (***Figure 5***) / 9 (channels per PD ***Olesen*** (***1979***); ***Liesche and Schulz*** (***2013***)) = 3.04 times as high density would be sufficient. These numbers are the same for straight PDs of any length. For calculating $\rho_{sn,neck}$, we assume that the sub-nano channel structure only occurs in the neck region, with an unobstructed sleeve with $R_c = R_{dt} + 2\bar{\alpha}$ in the central part. Using a homogeneous flux assumption around the transition between both parts, the factors x reduce to $x(2\tilde{l} + (1 - 2\tilde{l})/x)/l$. Similarly, ρ_{gate} is computed by assuming a 1 nm thick sub-nano channel structure at both ends of the PD.

As f_{ih} is affected by R_n and R_n values get quite large in our calculations with ρ fixed, we follow a different approach for computing $\bar{\alpha}_{sn}$ and $R_{n,sn}$ based on a given ρ. We use forward calculations based on 9 cylindrical channels in a PD, with the trapping rate κ_w adjusted with an outer radius R'_n that would fit all nine channels surrounding the DT.

$$\kappa_{w9} = 4\rho D H_c(\alpha / R'_n) R'_n \xi f(\rho\pi \tilde{R}'^2_n), \tag{27}$$

where $\tilde{A}_n$ is the surface area per cylindrical channel and $\xi = \frac{9(\bar{\alpha}-\alpha)^2}{\tilde{R}'^2_n}$ is the fraction of the enveloping circle that is occupied by the 9 channels. For sufficiently small $\bar{\alpha}$, the nine circular channels and minimal protein spacers (at least 1 nm wide) all fit while touching the DT. In that case: $R'_n = R_n = R_{dt} + 2\bar{\alpha}$. With $R_{dt} = 8$ nm, this is possible up to $\bar{\alpha} \approx 3.4$ nm. For larger $\bar{\alpha}$, the spacer requirement determines the outer radius of the composite of 9 channels and $R'_n = \bar{\alpha} + \frac{\bar{\alpha}+s/2}{\sin(\pi/9)}$, where $s = 1$ nm is the spacer width. R_{dt} does not occur in this equation, because the cylindrical channels can no longer (all) touch the DT.

A

$P(CF)$(μm/s)	$\bar{\alpha}$ (nm)	R_n (nm)	ρ (PD/μm^2)	ρ_{sn}	$\rho_{sn,neck}$	ρ_{gate}
6	2.0	12	33.5	139.9	87.8	36.7
	2.5	13	22.7	69.1	46.4	24.1
	3.0	14	16.8	40.9	29.1	17.5
	3.4	14.8	13.8	29.1	21.6	14.2
	3.5	15+	13.2	27.0	20.2	13.6
	4.0	16+	10.7	19.2	15.0	10.9
8.5	2.0	12	47.2	197.1	123.7	51.7
	2.5	13	32.0	97.4	65.4	34.0
	3.0	14	23.7	57.7	41.0	24.7
	3.4	14.8	19.4	41.1	30.5	20.1
	3.5	15+	18.5	38.1	28.5	19.1
	4.0	16+	15.0	27.0	21.1	15.4

B

$P(CF)$(μm/s)	ρ	$\bar{\alpha}$	R_n (nm)	$\bar{\alpha}_{sn}$*	$R_{n,sn}$ (nm) no spacers	$R_{n,sn}$ 1 nm spacers
6	10	4.2	16.3	5.2	18.4+	21.8
	13	3.5	15.1	4.6	17.3+	19.6
8.5	10	5.2	18.4	6.0	20.1+	25.2
	13	4.4	16.8	5.4	18.7+	22.5
1	10	1.5	11.0	2.6	13.2	13.2
	13	1.3	10.6	2.4	12.7	12.7

C

$P(CF)$(μm/s)	ρ	p	$\bar{\alpha}$	R_n (nm)	$\bar{\alpha}_{sn}$*	$R_{n,sn}$ (nm) no spacers	$R_{n,sn}$ 1 nm spacers
25	**10**	**1**	**10.5**	**28.9**	**10.0**	**28.0+**	**40.7**
	20	1	6.6	21.2	7.1	22.2+	29.4
		2	7.2	22.5	7.5	23.1+	31.1
	30	1	5.1	18.1	5.9	19.8+	24.6
		3	5.6	19.2	6.3	20.6+	26.3
	40	1	4.2	16.4	5.2	18.4+	21.8
		4	4.6	17.2	5.5	19.0+	23.1
	13	**1**	**8.8**	**25.6**	**8.8**	**25.5+**	**35.9**
	26	1	5.6	19.1	6.3	20.6+	26.2
		2	6.0	20.0	6.6	21.2+	27.3
	39	1	4.3	16.6	5.2	18.5+	22.1
		3	4.6	17.2	5.5	19.0+	23.1
	52	1	3.6	15.1	4.6	17.3+	19.6
		4	3.8	15.5	4.8	17.6+	20.4

Appendix 5 Table 1. Parameter requirements for reproducing measured $P(CF)$ values based on the default unobstructed sleeve model (also in ***Table 1***) and the sub-nano channel model. A: Required density (ρ) given $\bar{\alpha}$ and corresponding neck radius (R_n). B: Required $\bar{\alpha}$ and corresponding R_n given ρ. For $P(CF) = 25\mu$m/s, also values for a 2x, 3x and 4x increase of ρ are computed. This is done both for a uniform increase of the density ($p = 1$) and for (repeated) twinning ($p > 1$) from a uniform starting density (indicated in bold). A, B: The + sign at R_n indicates that the stated R_n is too narrow to fit nine sub-nano channels that touch a DT with $R_{dt} = 8$ nm. Models used for calculating required densities: ρ, R_n: default unobstruced sleeve model, ρ_{sn}, $R_{n,sn}$: sub-nano channel model, $\rho_{sn,neck}$: sub-nano channel model restricted to the neck regions ($l_n = 25$ nm), and ρ_{gate}: 1 nm thick structures at both PD entrances locally similar to the sub-nano channel model. *: $\bar{\alpha}_{sn}$ is calculated using R_n that allows for 1 nm spacers. C: p is the number of PDs per pit. This table was generated using PDinsight.

Appendix 6

PDinsight

PDinsight is written in python 3. It also depends on the numpy module. The program has different modes for computing the parameter requirements for a given $P(\alpha)$ and related quantities. The different modes and the relevant parameters are controlled from a parameter file (default: parameters.txt).

For electron microscopists, who typically have access to many ultrastructural parameters, but often do not know $P(\alpha)$, the mode `computeVals` will be useful. This computes the expected $P(\alpha)$ values when taking all parameters at face value. Comparison with the sub-nano channel model is possible. In principle, all model parameters must be defined, but missing parameters may be explored using lists of possible values or left at a default (e.g., cell length L and a triangular distribution of PDs), as these have little influence on $P(\alpha)$.

In tissue level experiments, $P(\alpha)$ is typically measured, but not all ultrastructural parameters will be known. It is likely that PD density ρ and radius (R_n, assuming straight channels) are poorly known. In this case, mode `computeRnDensityGraph` will be useful, or a combination of modes `computeDens` and `computeAperture` and a number of guesses for R_n/α or ρ, respectively. Additional poorly known parameters can be explored as suggested above. If uncertain, it is strongly advised to explore PD length l (≈cell wall thickness). For thick cell walls ($l \geq 200$ nm), it may be worth exploring the effects of increased central radius ($R_c > R_n$). This is currently only possible in mode `computeVals`.

Major modes

: The core of PDinsight is computing effective permeabilities ($P(\alpha)$) for symplastic transport based on all model parameters mentioned in the manuscript. This is in mode `computeVals`. The same computations are used in other modes, which compute the requirements for obtaining a given target value (or set of values) of $P(\alpha)$. In mode `computeDens`, required densities (ρ) are computed for given values of maximum particle size $\bar{\alpha}$ (and other parameters). In mode `computeAperture`, required apertures, given as $\bar{\alpha}$ as well as neck radius R_n, are computed for given values of ρ (and other parameters). In mode `computeRnDensityGraph`, R_n, ρ curves are computed that together yield a target $P(\alpha)$. The corresponding values of $\bar{\alpha}$ are also reported. These curves can be visualized using any plotting program.

Auxillary modes

: In computing $P(\alpha)$, correction factor f_{ih} is automatically included. For specific cases such as modelling studies, however, it may be useful to calculate f_{ih} separately. For this purpose, several modes exist for exploring inhomogeneity factor f_{ih}: `computeFih_subNano` (function of $\bar{\alpha}$; also output values for sub-nano model), `computeFih_pitField_dens` (function of ρ), `computeFih_pitField_xMax` (function of $\bar{\alpha}$) and `computeTwinning` (function of ρ_{pits}, cluster density).

By default, computations are performed for the unobstructed sleeve model. Most computations can also be performed for the sub-nano channel model ***Liesche and Schulz*** (***2013***). Using switch `compSubNano`, values for the sub-nano model are also computed.

Command line usage: python PDinsight.py PARAMETERFILE.

All outputs are tab separated files.

The latest version of PDinsight + documentation can be downloaded from [RELEASED UPON ACCEPTANCE].

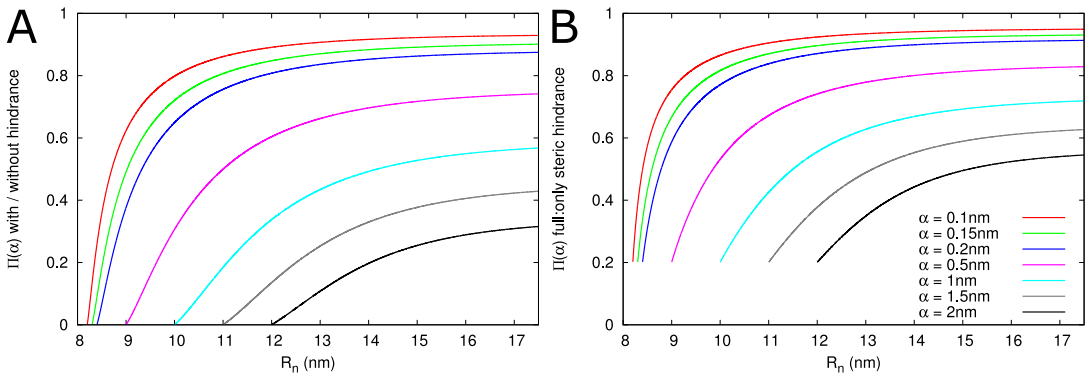

Figure 3–Figure supplement 1. A: Impact of hindrance on $\Pi(\alpha)$ decays with decreasing relative particle size. B: Steric hindrance alone particularly overestimates $\Pi(\alpha)$ for large relative particle sizes. Parameters: $l = 200nm,\ l_n = 25nm,\ R_{dt} = 8nm,\ R_c = 17.5nm$.

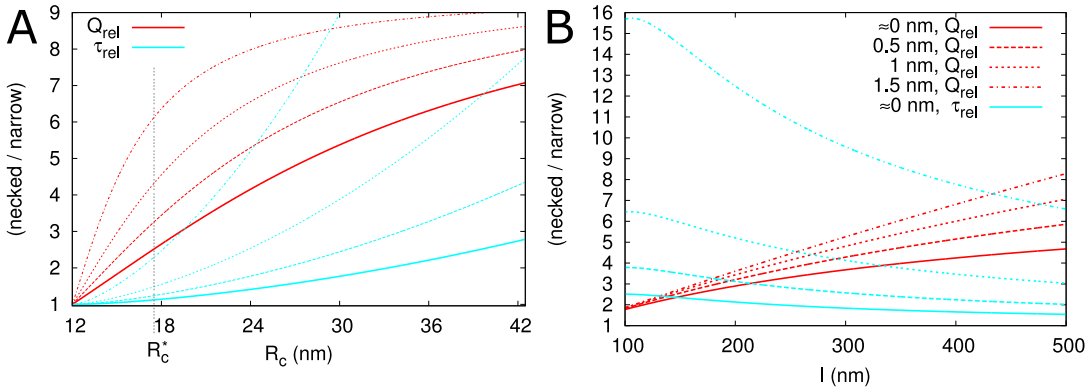

Figure 4–Figure supplement 1. Additional panels for **Figure 4**: Impact of central region dilation on molar flow rate (Q) and mean residence time (τ). A: R_c variable, $l = 500$ nm, compare to **Figure 4**A,B. B: $R_c = 26.4$ nm, l variable, compare to **Figure 4**C.

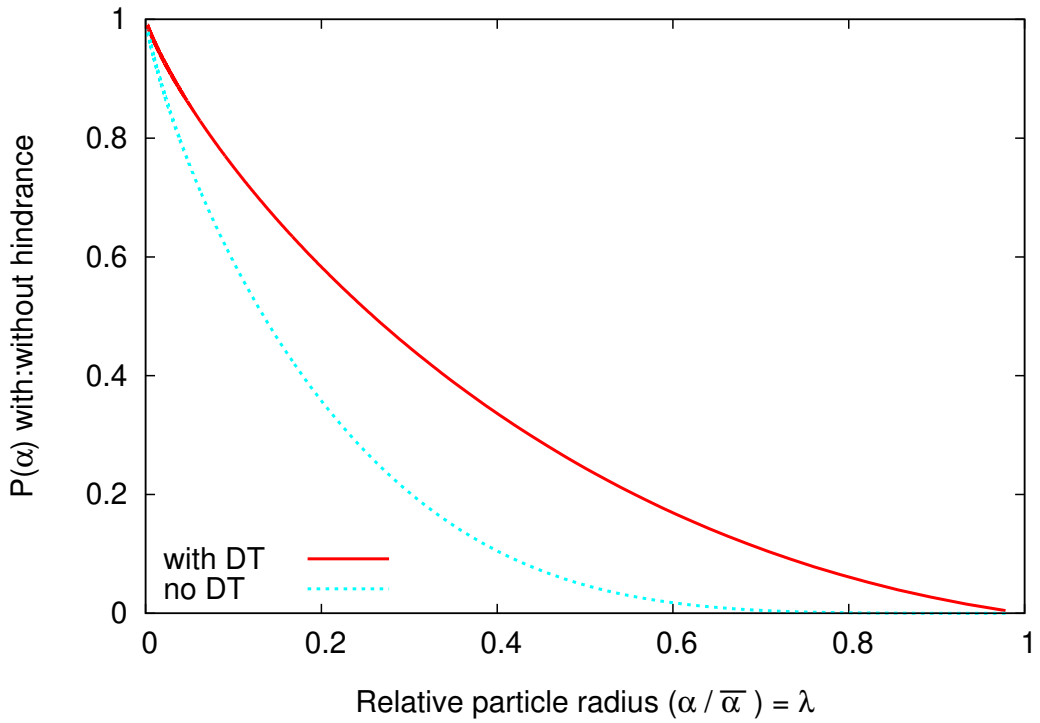

Figure 5–Figure supplement 1. Hindrance factors for slit ("with DT") and cylinder ("no DT") compared.

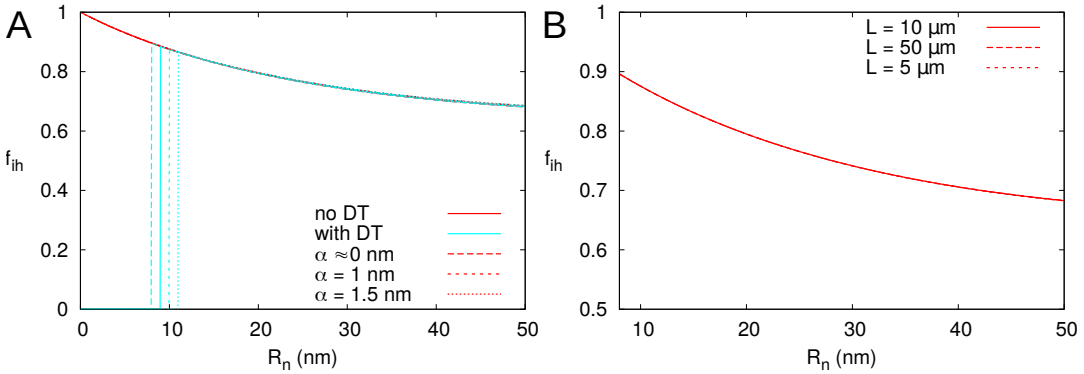

Figure 6–Figure supplement 1. f_{ih} is represented as a function of R_n, calculated for PDs with (cyan; A only) and without (red) DT. In all cases, solid lines correspond to: $l = 100$nm, $L = 10\mu$m, $\alpha = 0.5$nm, a PD density of $\rho = 10$ PD/μm^2, and PDs distributed on a triangular grid. Broken lines show the effects of changes in particle size α (A) or cell length L (B). Vertical cyan lines in A indicate the R_n in which f_{ih} is start to be measurable as determined by $\alpha < \tilde{\alpha}$.